J. Fluid Mech. (2016), *vol.* 787, *pp.* 50–83.
doi:10.1017/jfm.2015.599

The effects of forced small-wavelength, finite-bandwidth initial perturbations and miscibility on the turbulent Rayleigh–Taylor instability

M. S. Roberts[1,†] **and J. W. Jacobs**[1]

[1]Department of Aerospace and Mechanical Engineering, University of Arizona, Tucson, AZ 85721, USA

(Received 17 March 2014; revised 3 October 2015; accepted 12 October 2015;
first published online 7 December 2015)

Rayleigh–Taylor instability experiments are performed using both immiscible and miscible incompressible liquid combinations having a relatively large Atwood number of $A \equiv (\rho_2 - \rho_1)/(\rho_2 + \rho_1) = 0.48$. The liquid-filled tank is attached to a test sled that is accelerated downwards along a vertical rail system using a system of weights and pulleys producing approximately $1g$ net acceleration. The tank is backlit and images are digitally recorded using a high-speed video camera. The experiments are either initiated with forced initial perturbations or are left unforced. The forced experiments have an initial perturbation imposed by vertically oscillating the liquid-filled tank to produce Faraday waves at the interface. The unforced experiments rely on random interfacial fluctuations, resulting from background noise, to seed the instability. The main focus of this study is to determine the effects of forced initial perturbations and the effects of miscibility on the growth parameter, α. Measurements of the mixing-layer width, h, are acquired, from which α is determined. It is found that initial perturbations of the form used in this study do not affect measured α values. However, miscibility is observed to strongly affect α, resulting in a factor of two reduction in its value, a finding not previously observed in past experiments. In addition, all measured α values are found to be smaller than those obtained in previous experimental studies.

Key words: buoyancy-driven instability, nonlinear instability, turbulent mixing

1. Introduction

The Rayleigh–Taylor instability (RTI) is a buoyancy-driven fluid flow that occurs when a stratified system of unequal-density fluids is accelerated such that the light fluid is accelerated into the heavier one. In order for the instability to develop, the pressure gradient that results from the acceleration must be oriented such that $\nabla p \cdot \nabla \rho < 0$ (where p is pressure and ρ is density). The most notable example of the RTI occurs when a heavy fluid lies atop a light one while in the presence of a downward-acting gravitational force. However, RTI is also observed in situations

† Email address for correspondence: window59@hotmail.com

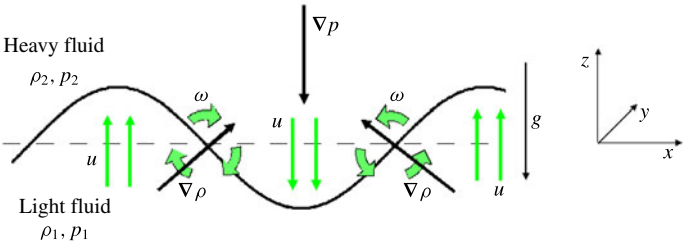

FIGURE 1. (Colour online) Visualization of an unstable Rayleigh–Taylor configuration where baroclinic torque at the interface creates vorticity and induces a velocity field that increases the baroclinic torque. Here ω is vorticity, p is pressure, ρ is density, u is velocity and g is gravity. The thick circular arrows represent the velocity field created by the vortex.

in which the fluid system itself is accelerated whereby the acceleration produces the necessary body force required to drive the instability.

RTI can be viewed to be the result of baroclinic torque created by the misalignment of the pressure and density gradients at the perturbed interface, as described by the two-dimensional inviscid vorticity equation

$$\frac{\mathrm{D}\omega}{\mathrm{D}t} = \frac{1}{\rho^2}\nabla\rho \times \nabla p, \tag{1.1}$$

where ω is vorticity, ρ is density and p is the pressure (Cohen & Kundu 2004). In this case the dominant pressure gradient is hydrostatic, resulting from the acceleration. When in the unstable configuration, for a particular harmonic component of the initial perturbation, the torque on the interface creates vorticity that will tend to increase the misalignment of the gradient vectors. This in turn creates additional vorticity, leading to further misalignment. This concept is depicted in figure 1, where it is observed that the two counter-rotating vortices have velocity fields that sum at the peak and trough of the perturbed interface. In the stable configuration, the vorticity, and thus the induced velocity field, will be in a direction that decreases the misalignment and therefore stabilizes the system.

A very important application of RTI is inertial confinement fusion (ICF). In ICF, a spherical capsule containing a deuterium/tritium (DT) mixture is bombarded with energy originating from high-powered lasers with the purpose of causing a fusion reaction to take place. The two isotopes fuse, producing ^{4}He, a neutron and energy (Ghasemizad, Zarringhalam & Gholamzadeh 2009). ICF experiments are currently being performed at the National Ignition Facility (NIF) at the Lawrence Livermore National Laboratory (LLNL), but ignition (a net output of energy from the fusion reaction) has not yet been achieved. RTI occurs at two instances during an ICF implosion and eventually causes turbulent mixing to take place. First, RTI occurs within the ablator region during the initial implosion of the target. Then, RTI occurs during the deceleration phase between the high-temperature, high-pressure DT gas and the outer, colder DT ice layer. The mixing due to RTI brings cold fuel from the outer layer into the centre 'hot spot', lowering the temperature and decreasing the reaction rate; this process may prevent ignition altogether (Betti *et al.* 1998; Herrmann, Tabak & Lindl 2001). By more fully understanding this instability, more efficient capsules can be designed (Clark *et al.* 2011).

The evolution of the RTI follows four main stages, as defined by Sharp (1984). In the first stage, if the perturbation amplitudes are small when compared to their wavelengths, the equations of motion can be linearized, resulting in exponential instability growth. In the early portion of this stage, a sinusoidal initial perturbation retains its sinusoidal shape. However, after the end of this first stage, when nonlinear effects begin to appear, one observes the beginnings of the formation of the ubiquitous mushroom-shaped spikes (fluid structures of heavy fluid growing into light fluid) and bubbles (fluid structures of light fluid growing into heavy fluid). The growth of the mushroom structures continues in the second stage and can be modelled using buoyancy drag models (Oron *et al.* 2001; Goncharov 2002), resulting in a growth rate that is approximately constant in time. At this point, nonlinear terms in the equations of motion can no longer be ignored. The spikes and bubbles then begin to interact with one another in the third stage. Bubble merging takes place, where the nonlinear interaction of mode coupling acts to combine smaller spikes and bubbles to produce larger ones. Also, bubble competition takes places, where spikes and bubbles of smaller wavelength that have become saturated are enveloped by larger ones that have not yet saturated. This eventually develops into a region of turbulent mixing, which is the fourth and final stage in the evolution. It is generally assumed that the mixing region that finally develops is self-similar and turbulent, provided that the Reynolds number is sufficiently large.

Lord Rayleigh (1883) was the first to study RTI, in which he analysed the stability of non-uniform density fluid in the presence of a gravitational field. In his analysis, Rayleigh considered both the case of two uniform fluids of different densities separated by a discontinuous interface and the case with an exponentially varying density distribution. Almost 70 years later, seemingly not aware of the analysis of Rayleigh, Taylor (1950) developed his own linear stability analysis of RTI. Following Taylor's work, a number of experimental studies were published (Lewis 1950; Emmons, Chang & Watson 1960; Cole & Tankin 1973; Ratafia 1973) focusing on the early-time linear stability analysis. Over the years the stability analysis of RTI has been expanded to include the effects of interfacial tension, viscosity (Bellman & Pennington 1954; Chandrasekhar 1961) and nonlinear effects (Fermi & Neumann 1955; Layzer 1955; Emmons *et al.* 1960; Jacobs & Catton 1988*a*,*b*). However, all of this early work focused on the evolution of the instability from a single-mode perturbation and thus only focused on the first two stages described by Sharp (1984).

This changed when experiments were published (Anuchina *et al.* 1978; Read 1984; Youngs 1984) where it was found that at late enough time the RTI appears to become turbulent, insensitive to its initial conditions and self-similar. The work of Anuchina *et al.* (1978) was compared to the theory of Neuvazhaev & Yakovlev (1976*a*,*b*). Anuchina *et al.* performed experiments where an initially stable light liquid above a heavy liquid configuration is accelerated downwards, by use of a gas gun, at a rate exceeding $100g$, causing the instability to develop. X-ray imaging was used to visualize the mixing region. In addition to experiments, Anuchina *et al.* also performed numerical simulations. Neuvazhaev & Yakovlev performed a full similarity analysis on the underlying equations of the turbulent velocity and concluded that the mixing-layer width should grow asymmetrically, where the bubble and spike grow at different rates. The growth is proportional to $f(n)g_{eff}t^2$, where $f(n)$ is a function of the density ratio. It was also found that the growth becomes symmetric as the density ratio of the two fluids becomes unity. The results of Anuchina *et al.* compared well to Neuvazhaev & Yakovlev's theory. Read's experiments were performed in a similar way, where an initially light over heavy fluid combination is made Rayleigh–Taylor

unstable by accelerating the fluid combination downwards at a rate greater than gravity. Using a rocket rig, the system was capable of producing accelerations up to $75g$. By using dimensional arguments and assuming the flow is self-similar, Youngs concluded that the mixing-layer width in this regime grows proportional to $Ag_{eff}t^2$.

Youngs went on to continue studying turbulent development RTI with simulations (Youngs 1989, 1991, 1994). Continuing with the experiments of Anuchina *et al.*, Kucherenko *et al.* (1991) investigated the turbulent RTI further using the gas gun apparatus with accelerations up to $650g$ (Kucherenko *et al.* 1997*a*,*b*, 2001). A few years later, Dimonte *et al.* (1996) performed similar experiments employing a linear electric motor (LEM) rig (Dimonte & Schneider 1996, 2000; Schneider, Dimonte & Remington 1998; Dimonte 2004; Dimonte *et al.* 2004; Dimonte, Ramaprabhu & Andrews 2007).

In experiments using a different approach, Snider & Andrews (1994), Ramaprabhu & Andrews (2003) and Mueschke *et al.* (2009) performed small-Atwood-number turbulent RTI experiments using gravity to drive the instability. These experiments were performed using a water channel where a heavier fluid is flowed atop a lighter one at the same velocity by means of a splitter plate, thus producing RTI. Unlike earlier highly accelerated turbulent RTI experiments, these lower-acceleration studies allowed the analysis of the interior of the turbulent mixing region, where velocity fluctuations could be extracted in which it was confirmed that fully developed turbulence had indeed been reached (Ramaprabhu & Andrews 2004). Gravitationally accelerated experiments with a small Atwood number were also performed by Linden & Redondo (1991), Dalziel (1993) and Jacobs & Dalziel (2005), where a tank with an initially heavy over light fluid configuration is separated by a horizontal barrier that is removed, thus creating RTI. These experiments also obtained measurements of the interior of the mixing region, showing that fully developed turbulence is indeed reached (Dalziel, Linden & Youngs 1999).

The focus of the present study is to experimentally determine the effects of initial perturbations and miscibility on the development of turbulent RTI. The experiments are performed in an apparatus developed at the University of Arizona (Waddell, Niederhaus & Jacobs 2001) that uses a weight-and-pulley system to accelerate an initially RTI stable configuration downwards at a rate greater than gravity to produce the instability. Of particular interest is to verify that the turbulent growth rate does not depend on the form of the initial conditions provided they are of sufficiently small wavelength as given by the bubble merger limit (Ramaprabhu, Dimonte & Andrews 2005).

Two methods of producing initial perturbations with the required short wavelengths are used. The experiments are either initiated with parametrically forced initial perturbations or are left unforced. The forced experiments have an initial perturbation imposed by vertically oscillating the liquid-filled tank to produce Faraday waves at the interface. The unforced experiments rely on random interfacial fluctuations, resulting from background noise, to seed the instability. The resulting instabilities resulting from both types of perturbations are then compared. Two different liquid combinations are used to produce either a miscible or immiscible combination, and the resulting instabilities from these different combinations are compared as well.

2. Experimental apparatus

Experiments were performed using a drop tower, in which a liquid-filled tank is accelerated downwards at a rate greater than gravity to produce the instability.

A square acrylic tank, having inside dimensions of 76 mm × 76 mm in the two horizontal directions and with a height of 178 mm, was used to contain the liquids. With this set-up, the aspect ratio is large enough that the instability should be unaffected by the top and bottom walls at the end of the self-similar stage, when the mixing-layer thickness is of the order of the tank width. At later times, one would expect a transition to $t^{2/5}$ growth, as found by Lawrie & Dalziel (2011). However, this regime is not the focus of the present study. The drop tower consists of two 102 mm × 102 mm, 3.05 m long, thick-walled vertical steel columns on which are mounted precision linear rails. Four Thompson Roundway linear roller bearings (two for each guide rail) are attached to a test sled that travels down the rails. The liquid-filled tank and imaging system are mounted to the test sled, which is made from Techno-Isel 30 mm × 250 mm extruded aluminium panels that have a system of slots that allow for easy fastening of the required instrumentation (Waddell 1999).

In order to accelerate the test sled downwards at a rate greater than that of gravity, a system of weights and pulleys is used (Waddell *et al.* 2001). Renderings of the set-up are shown in figure 4. A cable is fed through five pulleys so that the downward acceleration of the much more massive weight pulls the test sled downwards. This system is similar to a block-and-tackle system operated in reverse. The small distance traversed by the large mass is translated into a larger distance at the test sled, which acquires a larger velocity and acceleration. The mass of the weight-and-pulley system can be altered by changing the number of lead bricks contained in it and the corresponding weight can be increased up to approximately 450 kg, yielding a test sled acceleration of approximately $2g$. Subtracting the $1g$ downward acceleration due to gravity from the $2g$ acceleration experienced by the liquids results in a net acceleration of approximately $1g$. An I-beam is attached to the bottom of the test sled that provides the attachment point for the cable to direct its force through. At the bottom of the drop tower are two Enidine shock absorbers to stop the sled at the end of its travel. In addition to the shock absorbers, clay is used to add extra impact absorption. This deceleration system was chosen to keep the acceleration below $70g$, which is the camera's maximum acceleration limit.

It is necessary to have a method to quickly and repeatably release the sled initiated by an electronic trigger. To accomplish this, a release mechanism with an unstable linkage secures a 1/4 in. bolt attached to the test sled. The unstable linkage quickly releases the bolt when a small force is applied by a Dormeyer Industries P10-201L solenoid. Since only a small force is required for release, a P6-101L 'safety' solenoid is also used. This second solenoid effectively stabilizes the unstable linkage and must be disengaged before the test sled can be released. A SolidWorks rendering of the release mechanism is depicted in figure 2. More details of this mechanism can be found in Waddell *et al.* (2001).

A typical acceleration profile measured by an accelerometer that has been attached to the tank lid is shown in figure 3. An average through the main acceleration region between approximately 100 and 400 ms gives approximately $1g$ of acceleration. While time-dependent acceleration measurements were obtained for each experiment, only time averages over the main acceleration region were used in the analysis that follows.

The apparatus used in this study is identical to that used before (Olson & Jacobs 2009), but there have been instrumentation improvements. The 60 f.p.s. framing rate of the analogue camera used in the earlier studies has been upgraded with a faster 200 f.p.s. Pulnix TM-6740CL camera with 640 × 480 resolution and a Cameralink interface connected to a National Instruments PCIe-1427 frame grabber. This system provides more than a threefold increase in camera frame rate, thus increasing the

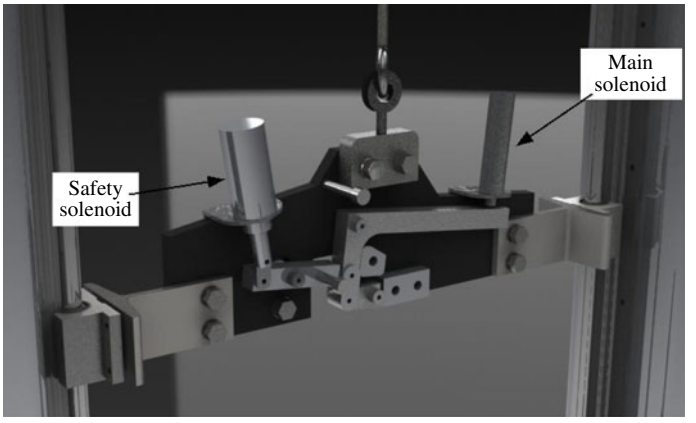

FIGURE 2. Rendering of the weight-and-pulley system release mechanism.

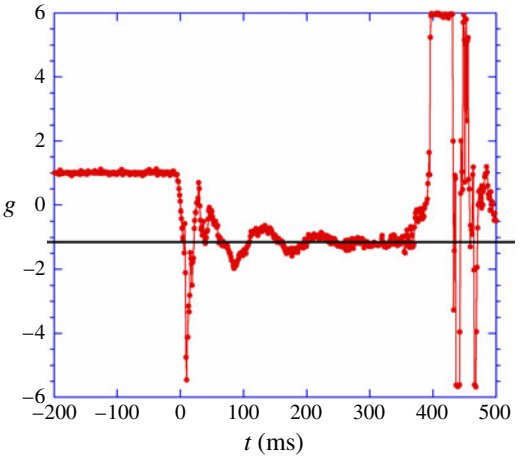

FIGURE 3. (Colour online) Typical acceleration profile during an experiment for the weight-and-pulley apparatus. The acceleration is represented in multiples of g (the ordinate) and time is represented as milliseconds (the abscissa).

temporal resolution of the data that can be acquired. In addition, the new camera has a bit depth of 10 bits rather than 8 bits, yielding a fourfold increase in greyscale resolution. A rendering of the test sled with the tank and camera attached is shown in figure 5.

Acceleration measurements are also acquired during each experiment. Two accelerometers were used: a Silicon Designs Model 2210-005 capacitive accelerometer with a $\pm 5g$ range and a PCB model JQ353-B32 constant-current piezoelectric accelerometer with a $\pm 100g$ range. The accelerometer measurements are used both for data analysis and to verify that the system is operating within its design limits. Data from the accelerometers are acquired and synchronized with the camera using a National Instruments PCIe-6251 multifunction Data Acquisition (DAQ) card.

3. Liquids and imaging

The experiments in this study were performed using either an immiscible or a miscible liquid combination, where care was taken to match both the Atwood number

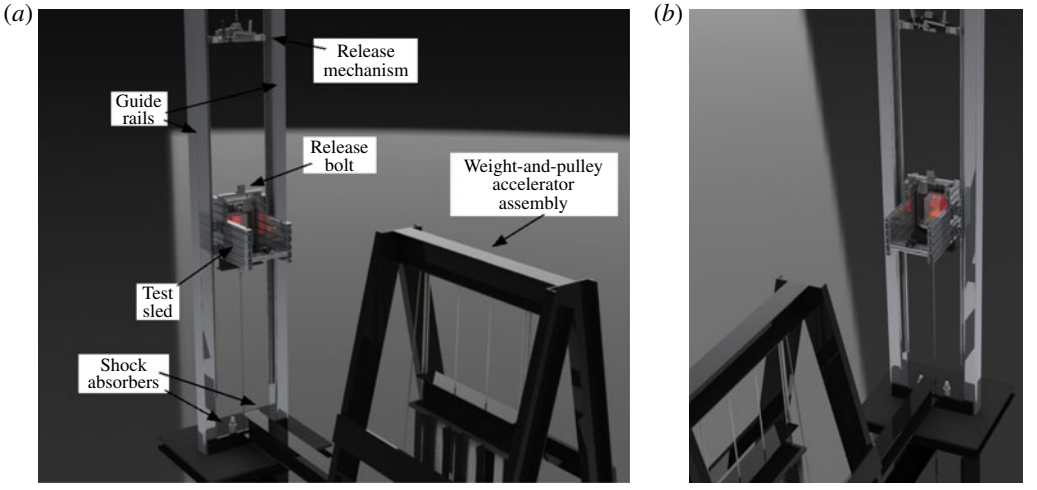

FIGURE 4. (Colour online) Renderings of the weight-and-pulley system.

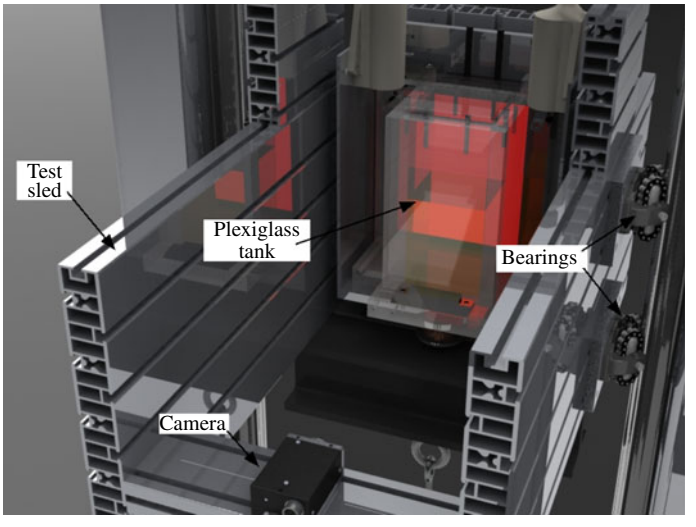

FIGURE 5. (Colour online) Rendering of the weight-and-pulley test sled with the experimental equipment attached.

and the viscosity so that only miscibility and forcing was varied. The Atwood number here was 0.48 for both of the fluid combinations. In accordance with viscous linear stability theory (Roberts 2012, A.31), the important quantity governing instability growth is the ratio of the dynamic viscosity difference to the sum of the densities. This quantity was matched to within 10 % for both the miscible and immiscible experiments (0.491 cSt for the miscible case and 0.496 cSt for the immiscible case). The immiscible combination consists of lithium polytungstate (LST Heavy Liquid) as the heavy liquid and silicone oil (Clearco 5cSt) as the light liquid. LST Heavy Liquid is a proprietary liquid solution consisting of a polytungstate salt water solution. The concentration of the salt (and thus the density) can be varied, but in the experiments presented here the solution was close to the saturation point. The silicone oil used

in this study was chosen because of its low viscosity and non-toxic properties. Surfactant was also added to the liquid combination to reduce the interfacial tension. The surfactant used in this study was AOT (dioctyl sulfosuccinate sodium salt). It should be noted that using surfactant to reduce the surface tension in mixing problems can produce unwanted effects in situations with large interfacial strain, such as occurs in the turbulent RTI. In these situations, highly strained regions of the interface may become depleted of surfactant, thus potentially locally increasing the surface tension. In order to mitigate this effect, a relatively large concentration of surfactant was used. Thus 1 g l^{-1} of AOT was added to the LST Heavy Liquid, and whatever did not dissolve was filtered out, thus assuring that the saturation limit was reached. Using this combination to achieve an Atwood number of 0.48, the LST Heavy Liquid was diluted to have a specific gravity of 2.61 and a viscosity of 6.34 cP (calculated using an exponential fit of the manufacturer's supplied data). The silicone oil has a specific gravity of 0.918 and a dynamic viscosity of 4.59 cP. Before an experiment, mixed liquids were allowed to equilibrate to room temperature by leaving them undisturbed overnight or longer.

For the miscible configuration, LST Heavy Liquid is used in conjunction with a 90 % ethanol–10 % water mixture. The use of large ethanol concentrations can lead to nonlinear mixing with the water-based heavy liquid solution, resulting in volume not being conserved during the mixing process. In fact, the liquid volume was observed to decrease during an experiment. Since the tank is rigid and sealed, this creates a vacuum, which causes the light liquid to cavitate and bubbles to form within the mixing region during an experiment. To prevent bubbles from forming, an ethanol mixture-filled bladder was affixed on the outside of the tank to provide a reservoir of fluid that could flow in through an opening as the volume decreases. It should be noted that this reduction in volume is consistent with what is observed with pure water mixing with alcohol, where the decrease in volume associated with water with pure ethanol to a 50 % mixture is 7.5 % (Parsons & Estrada 1942). Using this information, an estimate was derived to determine how much extra volume of liquid would be required for the heavy-liquid mixing case. Using the fact that the maximum mixing-layer width observed in the miscible experiments was approximately 40 mm and the tank has inside dimensions of 76 mm $\times$ 76 mm, the volume of the mixing region at the end of the experiment was 230 ml. Assuming that the 7.5 % reduction applies to this entire volume, this results in a 17 ml decrease. However, this value represents an upper bound and the actual required volume will be significantly less than this value. Note that this small volume should produce very minimal effect on the evolution of the instability. Although bubbles still occasionally formed, they were normally far enough from the interface not to affect the instability. Also, the bladder is situated at the top of the tank far from the interface to mitigate any effects on the RTI development.

Using LST Heavy Liquid in combination with a 90 % ethanol–10 % water mixture, an Atwood number of 0.48 was achieved. The LST Heavy Liquid was diluted to have a specific gravity of 2.31 and a viscosity of 3.02 cP (calculated using an exponential fit of the manufacturer's supplied data). In addition, pure ethanol was diluted with distilled water to a mole fraction of 0.735, yielding a specific gravity of 0.810 and a viscosity of 1.493 cP (as calculated from Tanaka *et al.* (1977)). Again, before the start of an experiment, mixed liquids were allowed to equilibrate to room temperature by leaving the liquids undisturbed overnight or longer.

The very large differences in the indices of refraction of the liquids used in this study precluded the use of planar imaging techniques. This resulted in backlit

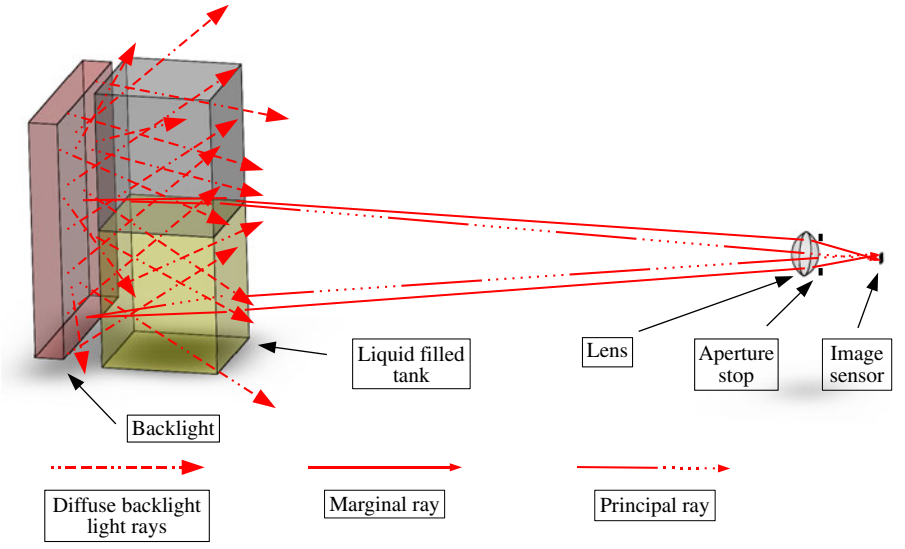

FIGURE 6. (Colour online) Illustration of the imaging system.

imaging being the only optical diagnostic possible for this study. Imaging was therefore accomplished by placing an LED backlight behind the tank and observing the resulting light transmission from the front, as shown in figure 6. Here the distance from the centre of the tank to the camera was 317 mm. Thus, parallax error was always less than 12 %.

When turbulent RTI experiments with unmatched refractive index are performed, the turbulent mixing region between the two pure liquids appears darker than the two pure liquids, making it visible during backlit visualization (Roberts 2012, 3.1.2). Since both fluids are nearly transparent, the mixing region becomes visible due to redirection of light from the refractive-index gradients within the turbid mixing region preventing light from the backlight from reaching the camera. This mechanism is a form of the shadowgraph principle when considering an extended light source (Settles 1999). It is also important to note that, as the number of refraction events that a light ray encounters increases, the mixed region will appear darker. Thus, smaller turbulent length scales will result in a darker-appearing mixing region. In all cases, the backlight and camera field of view extends beyond the tank sidewalls. Thus the horizontal extent of all images shown in what follows is always the full tank width.

In addition to the unmatched refractive-index experiments, it was found that, by using *trans*-anethole as the light liquid, it was possible to match the refractive index with LST Heavy Liquid in an immiscible combination. *trans*-Anethole is difficult to use owing to its ability to dissolve plastic. However, a small set of matched-index experiments were performed in order to validate the measurements from experiments having unmatched refractive index. Using this combination to achieve an Atwood number of 0.48, the LST Heavy Liquid was diluted to have a specific gravity of 2.81 and a viscosity of 10.21 cP (calculated using an exponential fit of the manufacturer's supplied data). The *trans*-anethole has a specific gravity of 0.988. Tests were also performed to confirm the validity of Beer's law for these experiments, and this can be found in Roberts (2012, 3.2).

4. Initial perturbations

Since it is desired to study the instability in the self-similar regime, small-wavelength initial perturbations when compared to the tank width are required (Cook, Cabot & Miller 2004). The self-similar flow is characterized by a progression in time from smaller to larger scales as the mixing-layer width grows in time. Scales cannot become larger than the tank width, and therefore self-similarity ends when the largest scale reaches that point. Thus, the initial perturbation wavelength must be small enough to allow sufficient time to study the self-similar flow. In the experiments presented here, the small initial perturbations imposed on the interface are either forced or left unforced where background noise acts as the source of the perturbations.

In the past, forced initial perturbations were created in our laboratory by horizontally oscillating the fluid-filled tank, which was affixed to a set of horizontal bearings (Waddell *et al.* 2001; Wilkinson & Jacobs 2007). This method works well to produce a large-wavelength perturbation (with a maximum of approximately five wavelengths spanning the tank width). However, when perturbations with greater than five wavelengths are produced, viscous damping results in amplitude non-uniformity, where the amplitude at the centre is less than that at the edges. An alternative method to produce interfacial perturbations is to parametrically (where gravity is the parameter being varied) excite the two stratified fluids to produce Faraday waves. This technique produces three-dimensional perturbations with uniform amplitude across the container. However, the perturbations produced are more complex and are no longer single-mode. This method was first implemented in this experimental set-up by Olson & Jacobs (2009) using a large stepper motor to oscillate the entire tank containing the liquids in the vertical direction. The production of large-wavenumber disturbances requires a higher frequency of oscillation that proved to be very difficult to accomplish with Olson's set-up. Also, the large mass of the motor resulted in large forces applied to connecting joints by the nearly $70g$ acceleration that occurs at the end of the experiment. Because of these difficulties, different mechanisms were considered and tested.

In order to determine the displacement of the tank oscillation amplitude necessary to create waves at the interface, an analysis of parametric wave theory was performed, and the details are available in Roberts (2012, A.3). It was determined that using a spring–mass system driven at resonance would be the best way to produce tank motion of this amplitude without using an exceedingly large motor. The tank and backlight are therefore mounted on an open enclosure that is affixed on the sides to the test sled using crossed roller bearings so that it is constrained to move only in the vertical direction. Equating the expression for Faraday-wave resonance frequency, $\omega_w = \sqrt{4kAg + \gamma k^3/(\rho_2 + \rho_1)}$, with that of the spring resonance frequency, $\omega_s = \sqrt{K/m}$, where K is the spring constant, m is the mass of the system, k is the wavenumber and γ is the interfacial tension, allows for the sizing of the required springs. The system uses three springs in parallel, which are held in place on the bottom of the open enclosure and the test sled. These springs provide a large enough spring constant to achieve the desired perturbation with approximately 20 wavelengths across the tank width. Small counterweights that can be adjusted in the front-to-back direction help balance the system and allow for fine tuning of the resonance frequency, allowing for up to an approximately 10 % variation in the resonance frequency. A voice coil is used to produce the force to drive the spring–mass system, allowing the acceleration amplitude to be easily adjusted without changing the frequency by

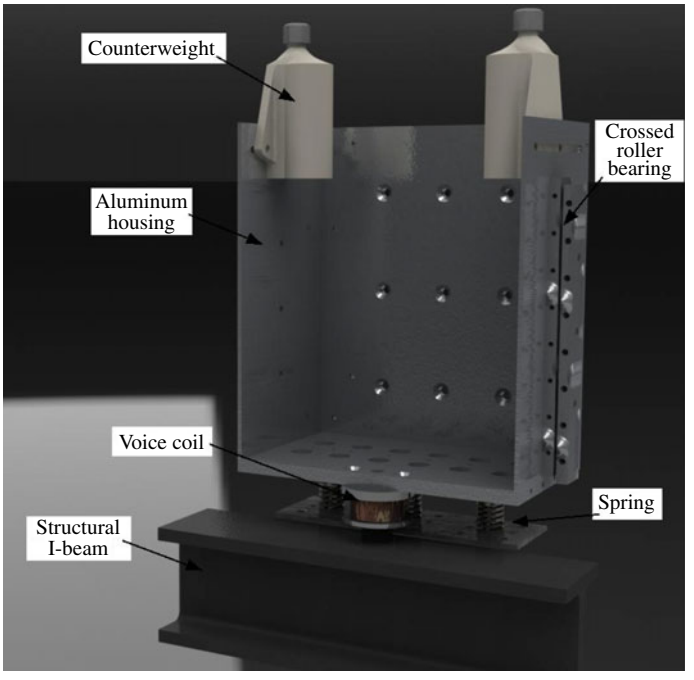

FIGURE 7. (Colour online) Rendering of the resonant enclosure used to create the vertical oscillations used for the parametric excitation.

increasing or decreasing the current passing through the coil. A rendering of the shaker system is shown in figure 7.

Parametrically forced immiscible and miscible experiments were performed. The smallest-wavelength perturbations that could be produced in the immiscible experiments with this set-up were approximately 3 mm, which required a forcing frequency of approximately 37 Hz. This is the initial perturbation that was used for all the experiments of this type presented in this study. The amplitude of the waves produced is approximately 0.5 mm. The sled release could not be synchronized with the tank oscillation, so each experiment was initiated at a different phase of oscillation. The visualization method used in these experiments did not allow measurement of perturbation spectra. However, the perturbation spectrum should be similar to that measured by Olson & Jacobs (2009), who utilized a similar forcing technique. In the forced miscible experiments, the tank was oscillated vertically at approximately 25 Hz, producing Faraday waves having an amplitude of approximately 1 mm and a wavelength of approximately 3 mm.

In the unforced experiments, the instability was allowed to evolve from background noise of unmeasurable size. However, the initial amplitude can be approximated using linear stability analysis. At an early time in the progression of the experiment, at the point where perturbations first become visible (at approximately 100 ms for the immiscible experiments and 175 ms for the miscible ones), the wavelength and amplitude were noted. Using this measured wavenumber and amplitude, along with the growth rate computed from viscous linear stability analysis, an approximate initial amplitude was determined by extrapolating backwards in time using the linear instability solution. The resulting initial amplitude, found using this technique, was

determined to be in the range of 1×10^{-7} to 1×10^{-6} m (for both miscible and immiscible experiments). It should be noted that the calculation of the predicted initial perturbation amplitude for the miscible case required the inclusion of the effects of a diffuse interface. It is known that diffusion reduces the initial growth rate of the RTI as shown by Duff, Harlow & Hirt (1962), which was accounted for in the calculated value for initial amplitude. For this calculation, an initial diffusion thickness of 0.5–1 mm was used as obtained by assuming that the development of the diffusion region grows as $\sqrt{Dt}$, and that 5–10 min has elapsed between the time when the tank was filled until when the experiment is performed. The diffusion coefficient used here (1.12×10^{-10} m^2 s^{-1} (Poling 2001)) is approximated by taking the average of the diffusion coefficients for ethanol into water and water into ethanol. Further details of this calculation can be found in Roberts (2012, 4.2.1).

It should also be noted that, while the form of the noise spectrum that resulted in the first observed perturbations is unknown, the many e-foldings that have occurred during this process result in a nearly single-scale perturbation at the fastest-growing wavelength. Thus, the primary difference between the forced and unforced experiments is the many orders-of-magnitude difference in the amplitude of the perturbations. In addition, forced experiments have a smaller wavelength with a smaller bandwidth, while the unforced experiments have a larger bandwidth centred around a wavelength that is slightly larger. However, in both cases we obtain a small-wavelength, finite-bandwidth initial perturbation that one would expect to result in the mode-coupling case described by Ramaprabhu *et al.* (2005).

One might expect components of the initial perturbation to be on the scale of the tank. However, in all of the experiments performed, none were observed, except for the effect of slight tilting of the tank with respect to the vertical direction. This tilting, which was impossible to remove entirely, produces the equivalent of a very small-amplitude triangular perturbation. In the cases with forced perturbations, the effects of this triangular perturbation are much less than that of the much faster-growing shorter-wavelength forced perturbation and thus are not observable. However, in the cases with unforced perturbations and particularly those with miscible fluid combinations that have much slower growth rates, the effects of tilting are more pronounced. But, nevertheless, they are always confined to regions near the walls.

5. Results and discussion

5.1. *Qualitative results*

For the immiscible experiments performed in this study, the fluids were initially added to the tank (heavy liquid first) with care taken to remove all air bubbles. Because the fluids remain unmixed, experiments were performed repeatedly without emptying the tank. Enough time was allowed to pass (approximately 10 min) between experiments to allow the emulsion layer that develops at the interface to dissipate. Shown in figure 8 is a sequence of images of a typical unforced immiscible experiment. It can be observed in this sequence that a range of scales develops at late time, beginning at approximately 300 ms, where both large and small wavelengths are observed. The initially small structures can be observed to merge into larger and larger structures as time progresses. Since a range of small scales is initially present, once the linear regime is no longer valid, nonlinear mode coupling will allow the creation of additional wavelengths, which is also observed. As the mixing-layer width becomes larger, so does the largest turbulent length scale, which is consistent with the concept of self-similarity. It should be noted that all experiments showed very

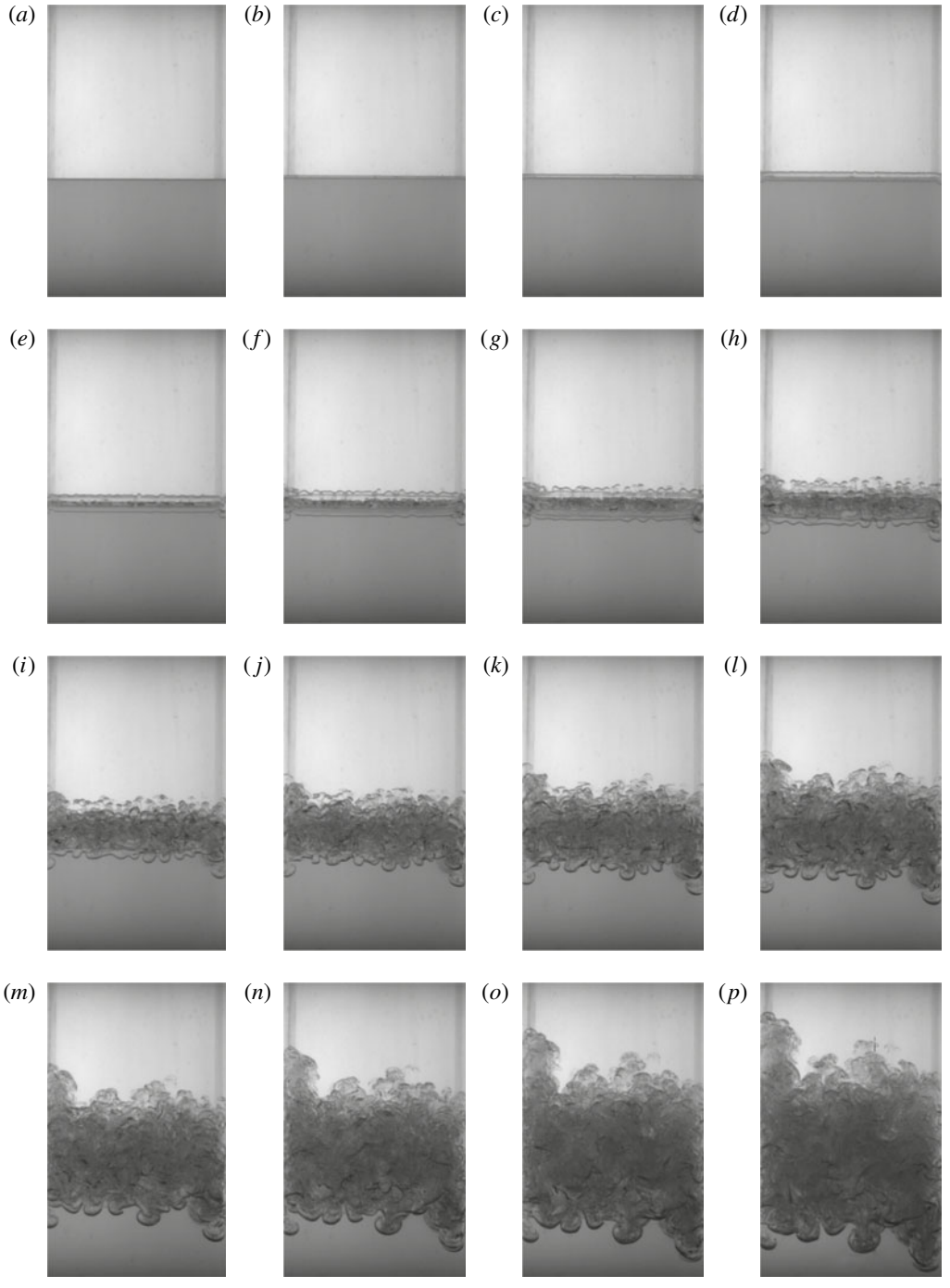

FIGURE 8. Experimental images progressing in time in which a diluted LST Heavy Liquid with AOT as a surfactant (bottom liquid) and 5 cSt silicone oil (top liquid) combination, giving an Atwood number of 0.48, was used. These experiments are unforced. Here the horizontal extent of the images is the full tank width (76 mm) at $t = 0$ ms (*a*), 25 ms (*b*), 50 ms (*c*), 75 ms (*d*), 100 ms (*e*), 125 ms (*f*), 150 ms (*g*), 175 ms (*h*), 200 ms (*i*), 225 ms (*j*), 250 ms (*k*), 275 ms (*l*), 300 ms (*m*), 325 ms (*n*), 350 ms (*o*) and 375 ms (*p*).

slight run-to-run variations, such as slight asymmetry or variation in the mixing-layer thickness across the tank width. However, these were not consistent from experiment to experiment and thus were assumed to be the result of randomness in the initial perturbation. For this reason, ensemble averages were used to obtain the mixing-layer widths along with the associated α values. Using the eigenvalue expression from a viscous linear stability analysis that includes the effects of interfacial tension to obtain the fastest-growing wavelength (Roberts 2012, A.31), one can estimate the interfacial tension of the fluid combination by assuming that the observed dominant wavelength at the onset of the instability is equal to the fastest-growing wavelength from the linear stability analysis. At a time of approximately 100 ms, the instability is still in the linear regime and a dominant wavelength of approximately 4.3 mm is clearly visible. Using this wavelength along with the known viscosities of the two liquids, the interfacial tension is found to be 2.1 mN m^{-1}. This value is also consistent with the value of 1.6 mN m^{-1} found for the heptane/calcium nitrate solution combination with AOT added that was used by Waddell *et al.* (2001).

Although it was expected that surfactant was required to produce small scales, an experiment was performed without surfactant to verify this assumption. In figure 9, an experiment with the same fluid combination and parameters as that used in figure 8 is presented, where the only difference is the lack of surfactant. In this experiment, only a few wavelengths across the tank were observed, and thus there is not enough domain size to display a large range of scales. Once again, an attempt to determine the interfacial tension was made using the experimentally observed wavelength. Although it was difficult to determine a dominant wavelength in this experiment, it was approximated to be 11 mm, which yields an approximate interfacial tension of 20 mN m^{-1}. Thus, adding surfactant appears to produce a factor of 10 decrease in the interfacial tension.

Figure 10 shows an immiscible experiment in which parametric forcing is used to produce the initial perturbation. It is observed that the initial wavelength is much less than the tank width. In addition, as with the unforced experiments (figure 8), there appears to be a large range of scales present at late time, as can be seen at 300 ms and later. The Faraday forcing used in this study does not produce a monochromatic initial perturbation. However, the perturbation that is produced has a bandwidth narrower than that which evolves from background noise. Therefore, the forced experiments might be expected to have a decreased amount of mode coupling when compared to the unforced experiments, which logically would result in a reduction in the degree of self-similarity observed. This difference, therefore, might be expected to affect the measured growth constant α. It is also apparent that the forced experiments develop into the possibly turbulent self-similar regime earlier than the unforced ones. With a larger initial amplitude, the forced experiments should be expected to progress into turbulence (and therefore self-similarity) more rapidly. All of these observations suggest that the effects of forcing on the growth of the turbulent mixing region deserve further study.

As with the immiscible experiments, miscible experiments were performed by first adding the heavy liquid and then the light one. Owing to the miscible nature of the liquids, a piece of balsa wood was rested atop the heavy liquid and allowed to float while the light liquid was added. This had the effect of spreading the liquid flow and thus decreasing the velocity to minimize mixing between the two fluids. Unlike with the immiscible experiments, the tank had to be refilled with new pure fluids after every experiment.

Shown in figure 11 is a sequence of images from a miscible unforced experiment. In these experiments, it is apparent that the first observable interfacial waves appear

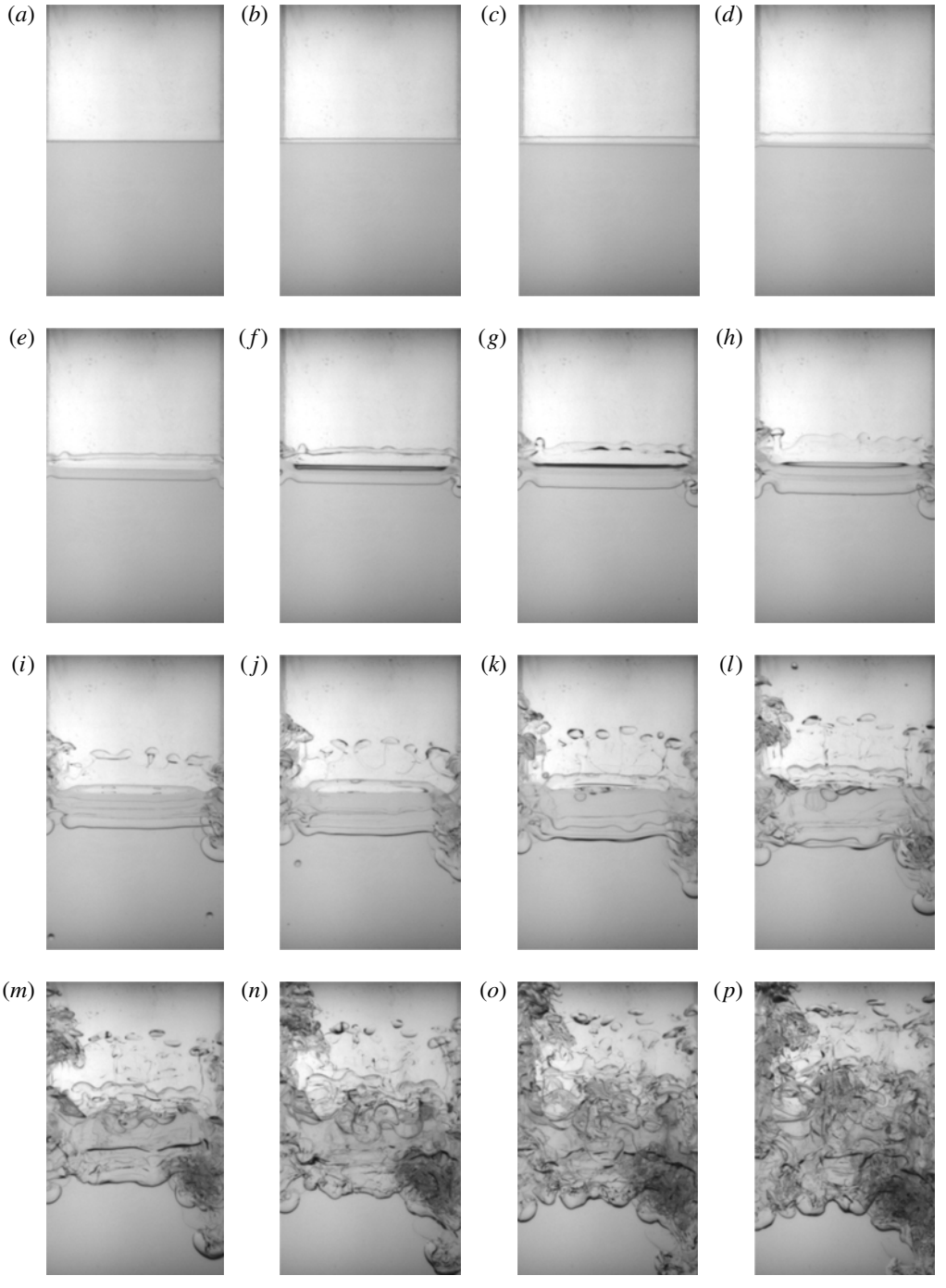

FIGURE 9. Experimental images progressing in time in which a diluted LST Heavy Liquid without a surfactant (bottom liquid) and 5 cSt silicone oil (top liquid) combination, giving an Atwood number of 0.48, was used. These experiments are unforced. Here the horizontal extent of the images is the full tank width (76 mm) at $t = 0$ ms (*a*), 25 ms (*b*), 50 ms (*c*), 75 ms (*d*), 100 ms (*e*), 125 ms (*f*), 150 ms (*g*), 175 ms (*h*), 200 ms (*i*), 225 ms (*j*), 250 ms (*k*), 275 ms (*l*), 300 ms (*m*), 325 ms (*n*), 350 ms (*o*) and 375 ms (*p*).

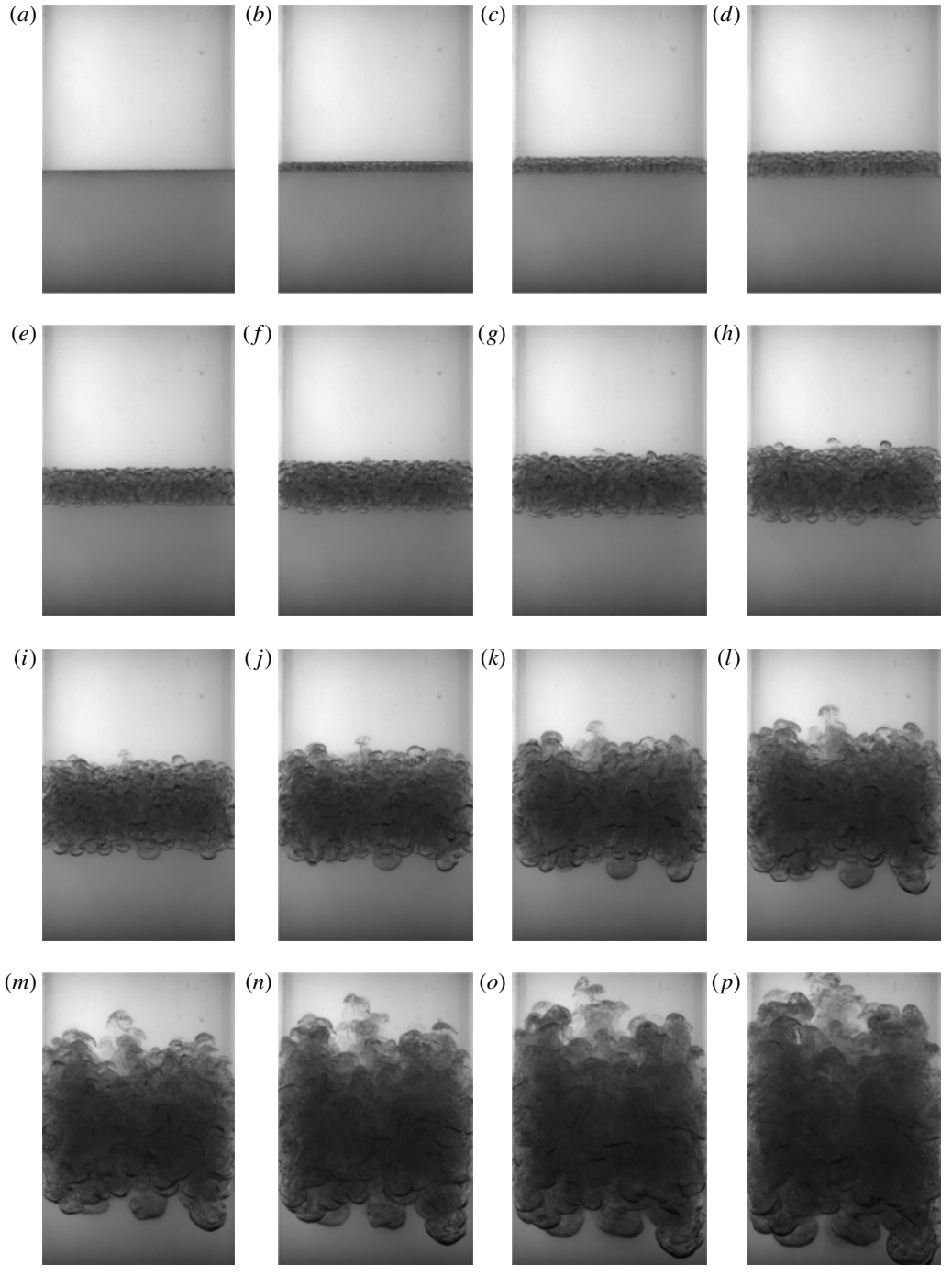

FIGURE 10. Parametrically forced experimental images progressing in time in which a diluted LST Heavy Liquid with surfactant (bottom liquid) and 5 cSt silicone oil (top liquid) combination, giving an Atwood number of 0.48, was used. Here the horizontal extent of the images is the full tank width (76 mm) at $t = 0$ ms (*a*), 25 ms (*b*), 50 ms (*c*), 75 ms (*d*), 100 ms (*e*), 125 ms (*f*), 150 ms (*g*), 175 ms (*h*), 200 ms (*i*), 225 ms (*j*), 250 ms (*k*), 275 ms (*l*), 300 ms (*m*), 325 ms (*n*), 350 ms (*o*) and 375 ms (*p*).

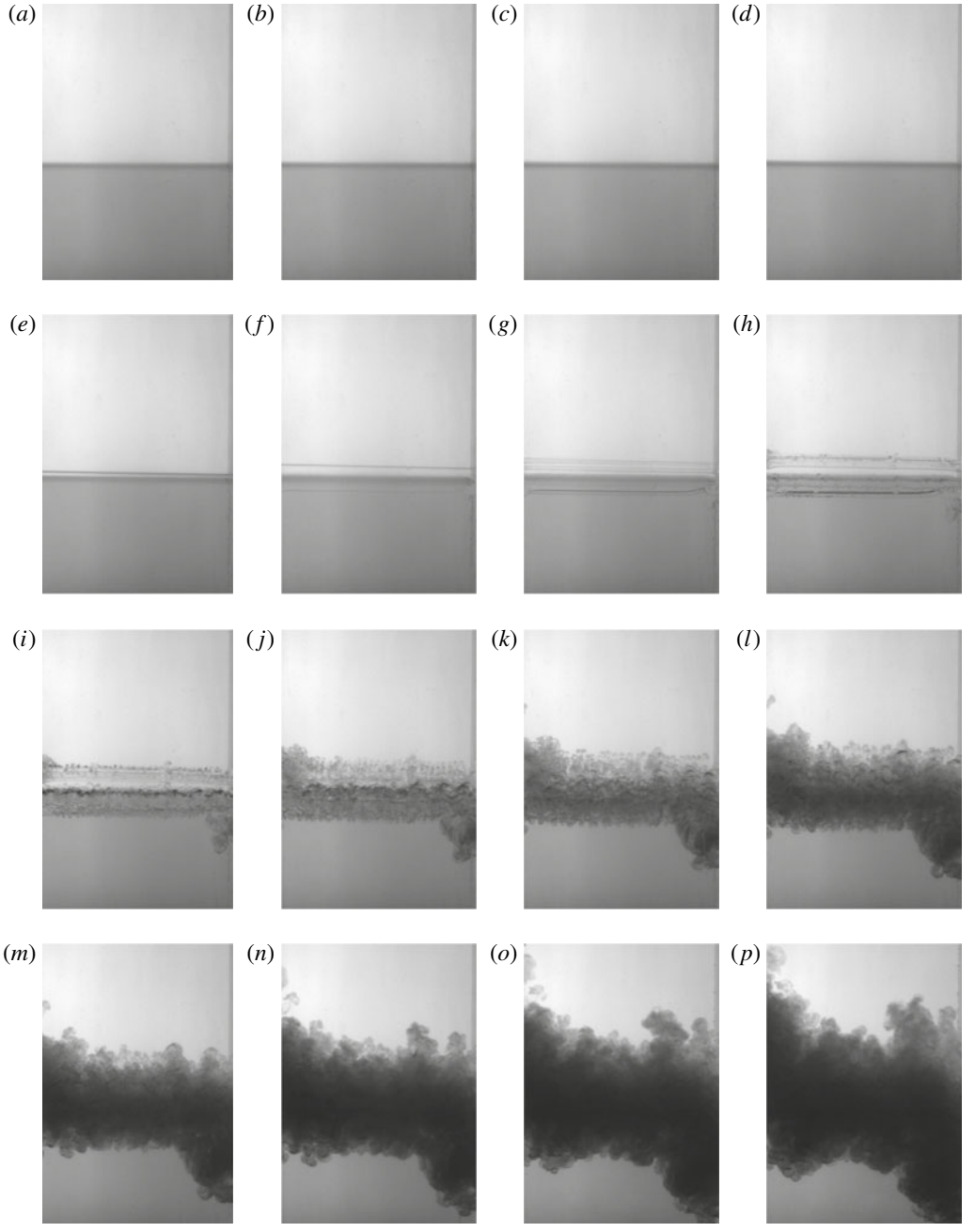

FIGURE 11. Miscible unforced liquid experiments performed on the weight-and-pulley apparatus with diluted LST Heavy Liquid (bottom liquid) and 90 % ethanol–10 % water (top liquid), having an Atwood number of 0.48. Here the horizontal extent of the images is the full tank width (76 mm) at $t = 0$ ms (*a*), 25 ms (*b*), 50 ms (*c*), 75 ms (*d*), 100 ms (*e*), 125 ms (*f*), 150 ms (*g*), 175 ms (*h*), 200 ms (*i*), 225 ms (*j*), 250 ms (*k*), 275 ms (*l*), 300 ms (*m*), 325 ms (*n*), 350 ms (*o*) and 375 ms (*p*).

after twice as much time has passed when compared to the immiscible experiments. In addition, these first observed perturbations appear to have a smaller wavelength than their immiscible counterparts and are of varying scale. It should be noted that a linear stability calculation including viscosity but neglecting diffusion yields a fastest-growing wavelength of 0.9 mm, which agrees well with that observed here. Adding diffusion to the analysis would further increase the fastest-growing wavelength, bringing it even closer to the observed value (1.8 mm). At late time, the development of a range of scales also is observed. Without the stabilizing effect of interfacial tension on small wavelengths, a larger range of wavelengths is present at late time. It is therefore more likely that the miscible experiments will have achieved true self-similarity because of the larger range of scales achieved.

In figure 12, a sequence of images from a forced miscible experiment is shown. In these forced experiments, it is observed that the growth of the mixing region develops nearly immediately, as was observed in the forced immiscible experiments. Similar to the immiscible experiments, at late time we also observe the development of a range of scales.

Shown in figure 13 is a comparison of the late-time behaviour of all four cases, all taken at a time in which the mixing-layer width is approximately the same. When comparing the two immiscible experiments, it is observed that the dominant wavelength (as observed in the profile of the bubble and spike fronts) appears similar in size, which is consistent with the assumption that forcing small wavelengths does not alter the flow once self-similarity is reached and implies that initial conditions do not influence the self-similar regime. Comparing the dominant length scales between the two miscible experiments yields a similar conclusion. However, one significant difference between the miscible and immiscible experiments is that the miscible experiments have noticeably darker mixing regions than the immiscible ones, thus implying that significantly smaller wavelengths are present in the miscible experiments than in the immiscible ones. Note that the lack of surface tension in the miscible experiments would allow the formation of smaller scales that would be suppressed by the presence of surface tension in the immiscible experiments. Thus the presence of shorter length scales is not the result of diffusion but instead is the result of the lack of surface tension. This observation, however, contradicts the fact that miscibility also results in molecular mixing, which should act to reduce refractive-index gradients. Thus the fact that the miscible experiments have darker mixing zones implies that the lack of surface tension is more dominant than the effect of diffusion.

5.2. *Quantitative results*

The primary measured quantity in this study is the mixing-layer width, h, and it is desired to determine how this quantity progresses in time. The mixing-layer width can be divided into that of the bubble (the portion in which the less dense mixing region grows into the heavy liquid), h_b, and that of the spike (the portion in which the more dense mixing region grows into the light liquid), h_s. The widths of the bubble and spike regions are found by subtracting the locations of the spike and bubble extents, respectively, from the initial interface location. Image analysis was performed using programs written in Java utilizing the ImageJ and JExcel libraries as the main components (Roberts 2012, 6.2).

The first step in the process was to obtain an intensity average across each row for each frame in the usable mixing region area. The usable mixing region area was determined by excluding structures created by interaction with the sidewalls of the

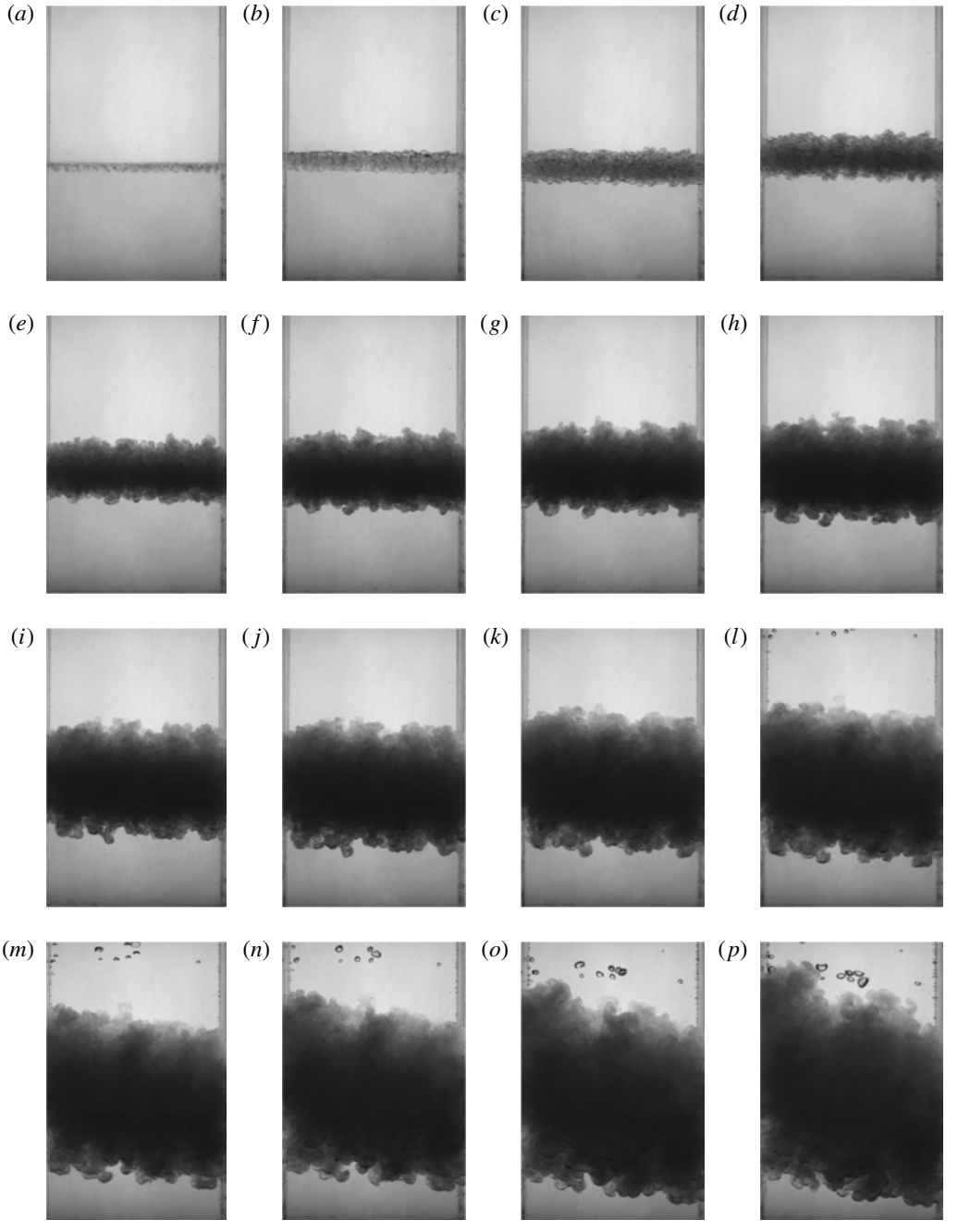

FIGURE 12. Miscible forced liquid experiments performed on the weight-and-pulley apparatus with diluted LST Heavy Liquid (bottom liquid) and 90 % ethanol–10 % water (top liquid), having an Atwood number of 0.48. The frequency of forcing here is 25 Hz. Here, the horizontal extent of the images is the full tank width (76 mm) at $t = 0$ ms (*a*), 25 ms (*b*), 50 ms (*c*), 75 ms (*d*), 100 ms (*e*), 125 ms (*f*), 150 ms (*g*), 175 ms (*h*), 200 ms (*i*), 225 ms (*j*), 250 ms (*k*), 275 ms (*l*), 300 ms (*m*), 325 ms (*n*), 350 ms (*o*) and 375 ms (*p*).

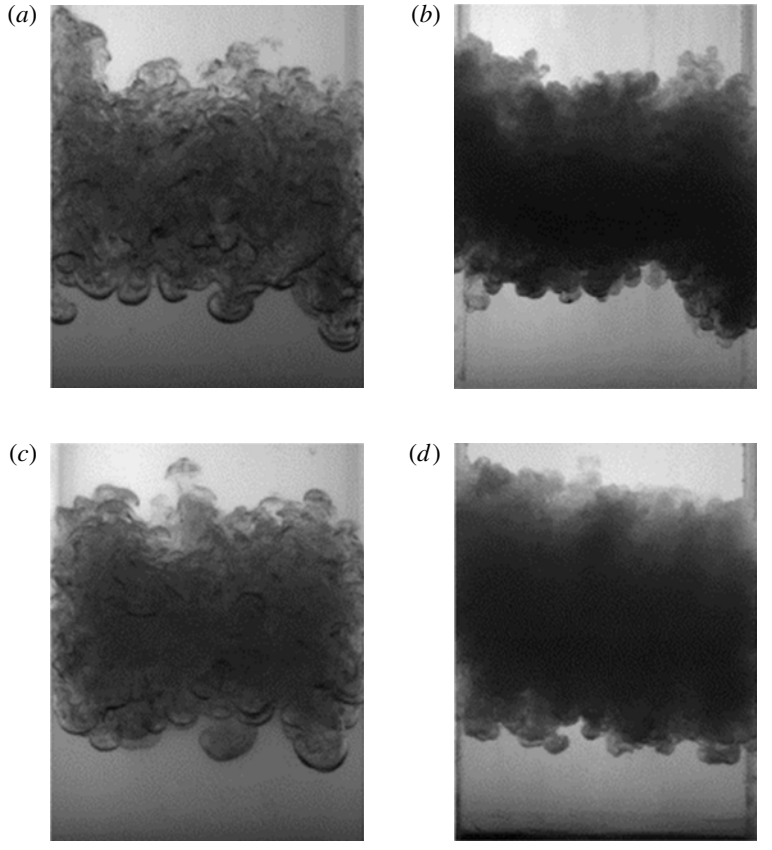

FIGURE 13. Comparison between forced, unforced, miscible and immiscible experiments performed on the weight-and-pulley apparatus for the 0.48 Atwood number case at $t =$ 320 ms for immiscible unforced (*a*), 380 ms for miscible unforced (*b*), 275 ms for immiscible forced (*c*) and 300 ms for miscible forced (*d*) cases. Images were chosen at times in which the mixing-layer width is approximately matched between experiments.

tank. At the latest usable frame for an experiment, the usable region was determined by excluding obvious wall effects, and this is the region used for averaging throughout the experiment. The mixing region width measurements also had to be measured while accounting for inhomogeneities in the tank and in the backlight. Ideally, one could divide each experimental image by an image in which the tank was empty to account for these non-uniformities. However, in addition to the backlight intensity being non-uniform in space, it was also found to vary in time due to temperature variations. For this reason, all of the experimental images for a particular run were scaled by the first image in the sequence and then the top and bottom fluid regions were re-multiplied by an average of a representative area of the corresponding fluid. This area was chosen to be near the interface to account for the backlight intensity variations that occur near the edges of each fluid.

It is important to point out that there is no standardized way of determining the mixing-layer width from backlit images such as used here. However, since we do not obtain concentration measurements, a consistent way of extracting the mixing-layer widths had to be developed. After the initial rescaling process has been performed, the data from each image were then row-averaged. Marching from both the light

and heavy liquid towards the interface, for the bubble and spike, respectively, the row-averaged intensity value is compared to the average intensity value in the pure liquid region. The edge of the mixing layer is determined when the intensity (I) drops below a threshold percentage value (P) defined by

$$I_{thresh} = I_{drk} + (I_{lght} - I_{drk}) \times \frac{P}{100}. \tag{5.1}$$

It was found that a threshold value of 80 % produces the most consistent results. Other threshold values (70 % and 90 %) were considered, but since they did not always yield a smoothly increasing mixing width across a set of experiments, they were not chosen. A 95 % threshold is often used in experiments in which concentration is measured, but this value showed inconsistent results in the present study and was thus found to be unsuitable. Also, because transmitted light intensity is not an indicator of concentration, using a 95 % threshold would not necessarily correspond to an equivalent concentration threshold. In figure 14, a montage of images is shown. Superimposed on each image are a scaled row-averaged profile along with horizontal lines indicating the determined edge locations found from using 70 %, 80 % and 90 % threshold values. Also, one line is present that represents the intersection of a least-squares curve fit of the intensity profile with the quiescent intensity value. Note that the evolution in time of the profiles appears to have the characteristics of self-similarity: as the profile becomes wider with time, its shape remains similar. It is obvious from the figure that using a 90 % or 95 % threshold value would result in only a slight increase in α. However, doing so would also bring with it significantly increased error due to increased run-to-run variation.

Plots showing the time evolution of mixing-layer width are shown in figure 15. Note that the parametrically forced experiments obtain a mixing-layer width larger than their unforced counterparts. As was shown in the image sequences, forcing produces larger-amplitude initial perturbations that also produce faster initial growth. Also, there is a very obvious difference between the immiscible experiments and the miscible ones. The miscible experiments grow significantly more slowly than the immiscible ones. This is to be expected since a diffuse interface will result in a reduction in the local Atwood number and thus growth rate as dictated by linear stability analysis.

We would like to determine the effects of forcing on the growth parameter α. We are not able to determine conclusively whether self-similarity is achieved in our experiments. However, since turbulence is required for self-similarity, it is useful to compute the Reynolds number in our experiments to determine whether it is at least as large as those of other studies that observed self-similar flow, i.e. the results of Dalziel *et al.* (1999) and Ramaprabhu & Andrews (2004). The Reynolds number obtained by Ramaprabhu & Andrews was approximately 1000. This value was calculated using

$$Re = \frac{h\dot{h}}{\nu}, \tag{5.2}$$

where h represents the full mixing-layer width and $\dot{h}$ is its temporal derivative. In the present study, bubble and spike Reynolds numbers are calculated individually,

$$Re = \frac{h_{b/s}\dot{h}_{b/s}}{\nu}, \tag{5.3}$$

so the corresponding Reynolds numbers of Ramaprabhu & Andrews becomes a factor of four smaller, yielding a value of 250. An approximate bubble Reynolds

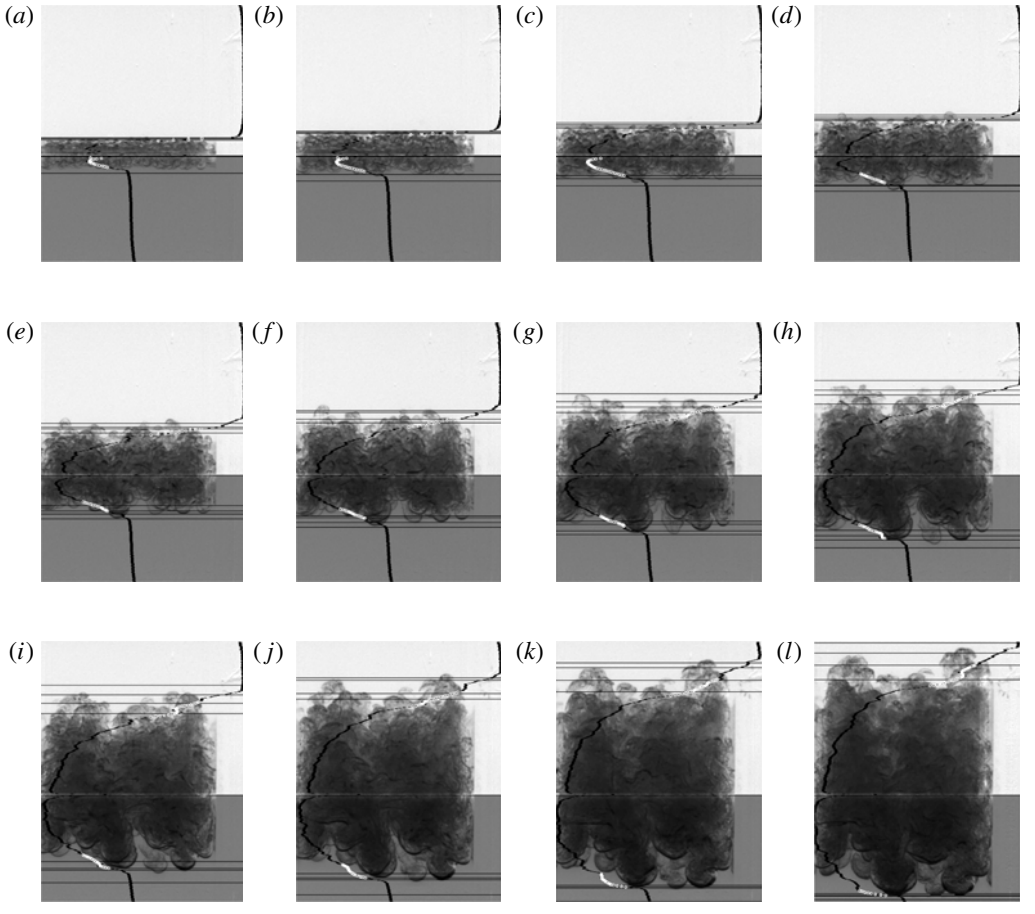

FIGURE 14. A sequence of images where the images of an ensemble-averaged refractive-index mismatch experiment have been post-processed. Horizontally averaged intensity values are superimposed on the images. The profiles have the characteristics of a self-similar flow as time progresses. Also on the images are horizontal lines representing different bubble and spike extent measurements so they can be compared. Times are (*a*) $t = 100$ ms, (*b*) $t = 125$ ms, (*c*) $t = 150$ ms, (*d*) $t = 175$ ms, (*e*) $t = 200$ ms, (*f*) $t = 225$ ms, (*g*) $t = 250$ ms, (*h*) $t = 275$ ms, (*i*) $t = 300$ ms, (*j*) $t = 325$ ms, (*k*) $t = 350$ ms and (*l*) $t = 375$ ms.

number in the experiments of Dalziel *et al.* at a time where the flow was verified, by internal mixing region measurements, to be turbulent was 3700 (Dalziel *et al.* 1999; S. B. Dalziel 2013, personal communication). Plots of Reynolds number versus time for the cases studied here are shown in figure 16. The approximate maximum values, excluding the scatter towards the ends of the experiments, are approximately 2000, 4000, 1500 and 4000 for the unforced immiscible forced immiscible unforced miscible and forced miscible experiments, respectively, where the values for the spikes are approximately 20 % larger than those for the bubbles. It is observed that the maximum Reynolds numbers for the forced experiments are twice those for the unforced ones. Since these values are larger than those obtained by Ramaprabhu & Andrews and similar to those of Dalziel *et al.* (both of whom found their flows to

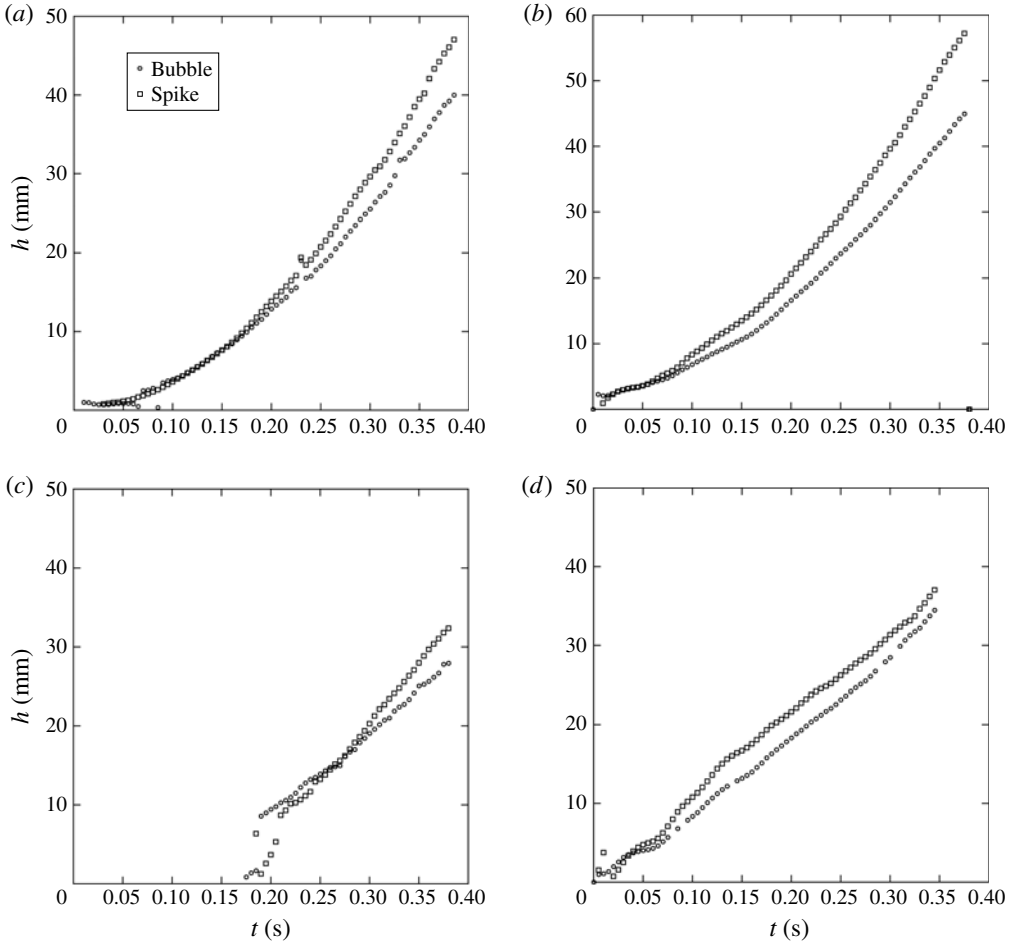

FIGURE 15. Mixing-layer width for ensemble-averaged experiments where 80 % of the pure liquid intensity was taken as the mixing-layer width cutoff. Data are for LST Heavy Liquid experiments for the four cases discussed previously: (*a*) immiscible unforced, (*b*) immiscible forced, (*c*) miscible unforced and (*d*) miscible forced.

be self-similar and turbulent by internal mixing-layer measurements), we will assume our experiments are self-similar.

Under the premise that we have a large enough Reynolds number to achieve self-similarity, we will proceed with the determination of the growth factor α. As shown by Dimonte & Schneider (2000), one way to measure α is to plot $\sqrt{h_{b/s}}$ versus $t\sqrt{Ag_{eff}}$ and fit a straight line (by the method of least squares) through the part of the curve that appears linear at late time. Squaring the slope of this line will yield an averaged value of α. Another way of determining α is to use a method proposed by Cabot & Cook (2006) using an expression developed by Ristorcelli & Clark (2004) where

$$\alpha = \frac{\dot{h}_{b/s}^2}{4Ag_{eff}h_{b/s}}. \tag{5.4}$$

This gives a time-dependent expression for α which can be compared to the average value.

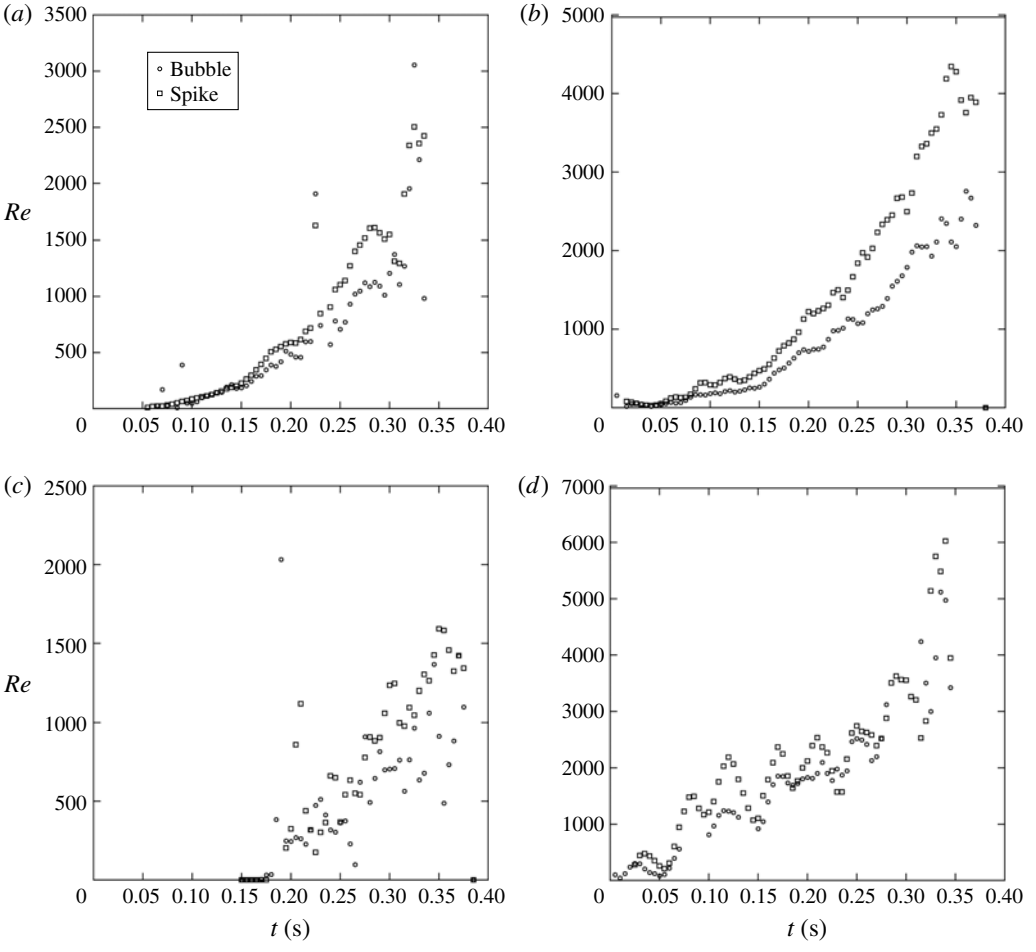

FIGURE 16. Reynolds-number data for ensemble-averaged experiments where 80 % of the pure liquid intensity was taken as the mixing-layer width cutoff. Data are for the four cases of the LST Heavy Liquid experiments: (*a*) immiscible unforced, (*b*) immiscible forced, (*c*) miscible unforced and (*d*) miscible forced.

5.2.1. *Immiscible experiments*

In using the fitting method for the calculation of α as used by Dimonte & Schneider (2000), it is desirable to employ a fixed fitting region for consistency in comparing values from different sets of experiments. For the immiscible fluid combination in the present study, the fitting region was chosen to be $5\ \text{mm}^{1/2} < t\sqrt{Ag_{eff}} < 25\ \text{mm}^{1/2}$ and the curve fits are shown in figure 17. For the α calculations, g_{eff} was found by averaging over the main acceleration region between approximately 100 and 400 ms, which yielded $11.06 \pm 0.02\ \text{m s}^{-2}$ for the unforced case and $10.87 \pm 0.33\ \text{m s}^{-2}$ for the forced case, where uncertainties represent 95 % confidence intervals of measurements from individual experiments. The calculated values of α are displayed on the plots. At the end of the unforced experiments, α is nearly constant, indicated by the linearity of the data at late time, with a value of 0.059 ± 0.002 for the spike and 0.047 ± 0.007 for the bubble. For the forced case, α is 0.057 ± 0.014 for the spike and 0.044 ± 0.009 for the bubble. These α values represent an ensemble

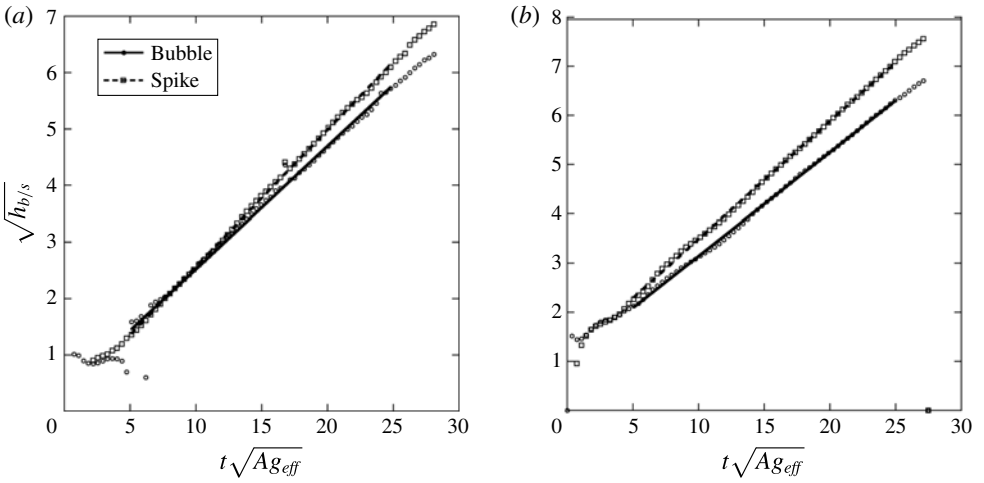

FIGURE 17. Measurements of α determined by fitting a straight line to the $\sqrt{h_{b/s}}$ versus $t\sqrt{Ag_{eff}}$ plot for ensemble-averaged experiments where 80 % of the pure liquid intensity was taken as the mixing-layer width cutoff. Data are for the two LST Heavy Liquid immiscible cases: (*a*) immiscible unforced; $\alpha^b = 0.047$, $\alpha^s = 0.059$ and (*b*) immiscible forced; $\alpha^b = 0.044$, $\alpha^s = 0.057$.

average of 13 experiments for the unforced case and 10 experiments for the forced case. Here the uncertainties were calculated using a 95 % confidence interval from α values determined from experiments analysed individually. Note that the α values obtained in both cases are smaller than those obtained in earlier experimental studies. For example, when comparing the experiments that match the Atwood number used in our experiments, Youngs & Read (1983) obtained α values of 0.086 and 0.066 for spike and bubble, respectively, Kucherenko *et al.* (1991) obtained values of 0.070 and 0.055, respectively, and Dimonte & Schneider (2000) obtained values of 0.063 and 0.050, respectively. However, it should be noted that the data of figure 17 have significantly greater time resolution and are an average over a much larger ensemble than in previous studies. As a result, the measurements shown in this figure yield much smoother curves than in the earlier experiments and thus could explain the small difference in α values measured here. In addition to attaining smaller α values than previously found, the results presented here indicate that imposing forced initial perturbations with a wavelength smaller than the fastest-growing wavelength and larger than the cutoff wavelength (as is done in the forced experiments) yields an α value similar to that obtained in the unforced experiments. The larger amplitude of the forced case extends the experimental time in the nonlinear regime for the flow to evolve, but the similar α values imply the extra evolution time is not necessary to achieve the same final result. The spike to bubble ratios are also very similar for the forced and unforced experiments, where the ratio α_s/α_b was found to be 1.26 ± 0.19 and 1.30 ± 0.41 for the unforced and forced cases, respectively. Here the error estimates were obtained by propagating error estimates from the bubble and spike values. These ratios compare well with past experiments having similar Atwood number, where Youngs & Read (1983) found a ratio of 1.3, Dimonte & Schneider (2000) found a ratio of 1.26 and Kucherenko *et al.* (1991) found a ratio of 1.27.

Using (5.4), α is plotted in figure 18, where $\dot{h}_{b/s}$ is determined using a central difference approximation and g_{eff} are the average values used in the $\sqrt{h}$ versus t

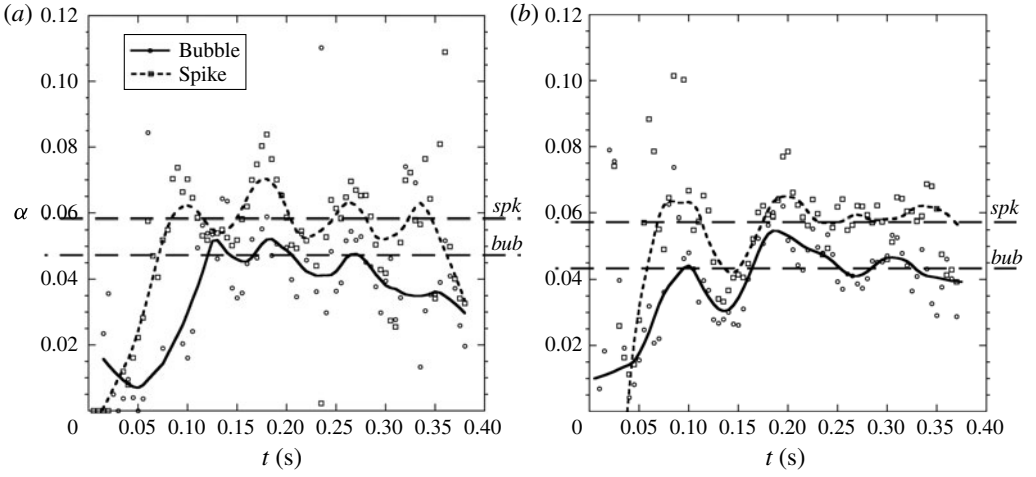

FIGURE 18. Measurements of α determined by the method of Cabot & Cook (2006) for ensemble-averaged immiscible experiments where 80 % of the pure liquid intensity was taken as the mixing-layer width cutoff. Here $\dot{h}_{b/s}$ was calculated using a central difference approximation. Data are for the two LST Heavy Liquid cases: (*a*) immiscible unforced and (*b*) immiscible forced. The horizontal line here represents α obtained from the square-root method and is drawn to show the consistency between methods of determining α: the top line represents the spike and the bottom represents the bubble for both plots. Also, a weighted running average of 20 % of the total number of points in the particular experiment is also performed (represented as solid and dashed lines on the plot) to smooth the data.

method described above. A weighted running average of α of 20 % of the total number of points in the particular experiment is also performed (represented as solid and dashed lines on the plot) to smooth the data. The weighted running average function performs a nonlinear regression using a locally weighted regression method, where more weight is given to the central data point. Horizontal dashed lines are also drawn representing the average α values obtained by the square-root method, described above, showing that it agrees well with (5.4) at late time. It is observed that α for the forced and unforced cases show similar values.

As mentioned above, in addition to the unmatched refractive-index experiments, a small set of experiments were performed using a liquid combination in which LST Heavy Liquid is the heavy liquid and trans anethole is the light liquid, where the refractive indices were matched. In addition, these experiments were unforced. The analysis of these experiments utilized Beer's law absorption to obtain integrated concentration profiles, from which the 10 % and 90 % concentration thresholds of LST Heavy Liquid were used to determine the spike and bubble front locations. From these, α measurements were obtained utilizing the same techniques as used in the unmatched-index experiments. For these matched-index experiments, α was found to have a value of 0.046 ± 0.011 for the spike and 0.039 ± 0.015 for the bubble. These α values represent an ensemble average of nine experiments. Here the uncertainties were calculated using a 95 % confidence interval from α values determined from experiments analysed individually. These measurements compare well with the non-index-matched experiments, thus validating our results. More information on these experiments can be found in Roberts (2012, 6.2).

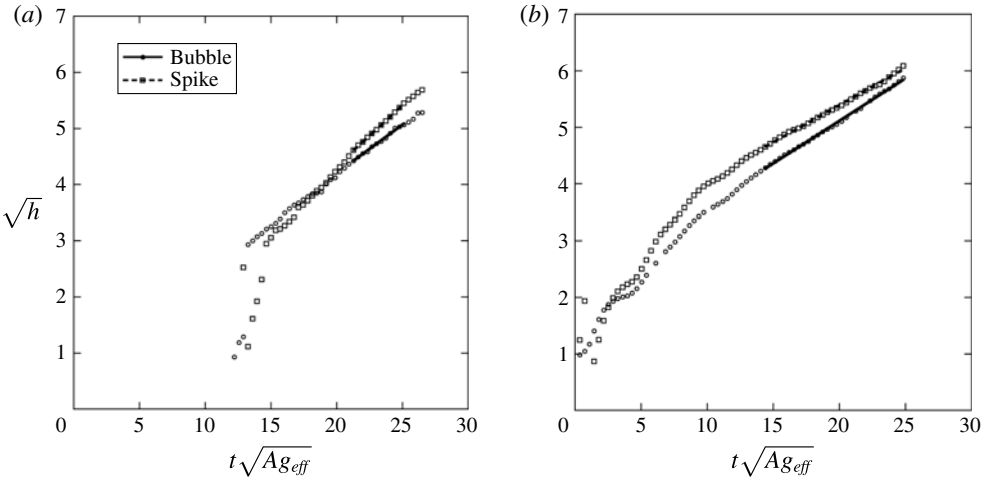

FIGURE 19. Measurements of α determined by fitting a straight line to the $\sqrt{h_{b/s}}$ versus $t\sqrt{Ag_{eff}}$ plot for ensemble-averaged experiments where 80 % of the pure liquid intensity was taken as the mixing-layer width cutoff. Data are for the two LST Heavy Liquid miscible cases: (*a*) miscible unforced; $\alpha^b = 0.030$, $\alpha^s = 0.047$ and (*b*) miscible forced; $\alpha^b = 0.023$, $\alpha^s = 0.017$.

5.2.2. *Miscible experiments*

The fitting region for the miscible experiments was chosen to be $15\ \text{mm}^{1/2} < t\sqrt{Ag_{eff}} < 25\ \text{mm}^{1/2}$, which is slightly later in time than for the immiscible experiments due to the difficulty in making measurements at early time. The curve fits for extracting α are shown in figure 19, where the values of α are displayed on the plots. For the α calculations, the average acceleration was computed and used for each set of experiments in the same manner as was done for the immiscible experiments. The acceleration for the unforced and forced cases is $10.12 \pm 2.21\ \text{m s}^{-2}$ and $10.73 \pm 0.34\ \text{m s}^{-2}$, respectively, where the uncertainties represent 95 % confidence intervals of measurements from individual experiments. These result in unforced spike and bubble α values of 0.047 ± 0.023 and 0.030 ± 0.008, respectively, and forced spike and bubble values of 0.017 ± 0.008 and 0.023 ± 0.007, respectively. These α values represent an ensemble average of nine experiments for the unforced case and nine experiments for the forced case as well. Again, the uncertainties here were calculated using a 95 % confidence interval from α values determined from experiments analysed individually. Thus, as was similarly found for the immiscible experiments, the α values obtained for the miscible experiments are smaller than those obtained in past experiments. But, unlike the immiscible experiments that yielded α values only slightly smaller than previous measurements, values for the miscible experiments are significantly smaller than those previously found. Thus the miscible experiments yield α values that are significantly less than those of their immiscible counterparts. Differences with the immiscible experiments' spike to bubble ratios for the growth rates are also observed. For the miscible unforced and miscible forced experiments, the ratio α_s/α_b was found to be 1.57 ± 0.87 and 0.74 ± 0.41, respectively. Here the error estimates were obtained by propagating error estimates from the bubble and spike values. Note that the forced miscible ratio is less than unity, indicating a larger bubble growth rate than for the spike. However, the very large error estimate associated with this value indicates that this discrepancy can probably be attributed to experimental uncertainty caused by imaging limitations.

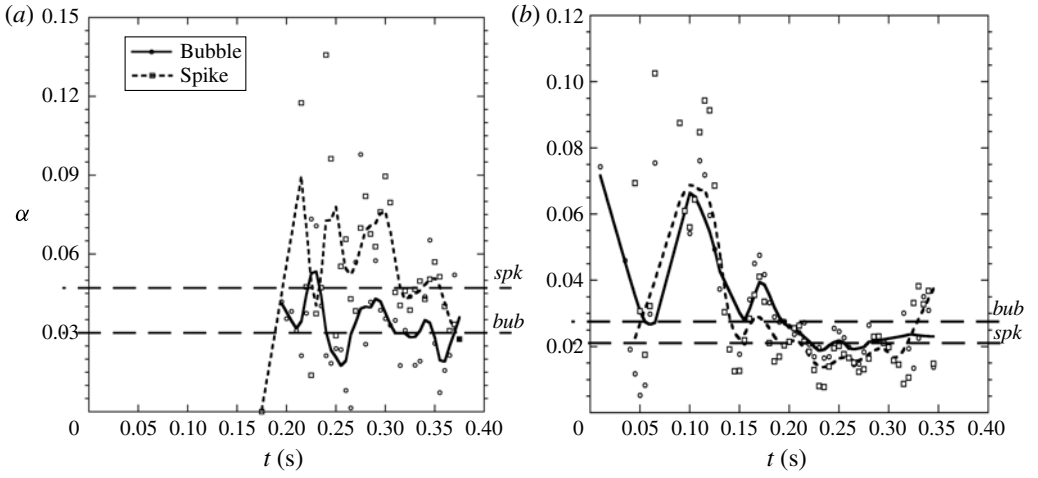

FIGURE 20. Measurements of α determined by the method of Cabot & Cook (2006) for ensemble-averaged miscible experiments where 80 % of the pure liquid intensity was taken as the mixing-layer width cutoff. Here $\dot{h}_{b/s}$ was calculated using a central difference approximation. Data are for the two LST Heavy Liquid cases: (*a*) miscible unforced and (*b*) miscible forced. The horizontal line here represents α obtained from the square-root method and is drawn to show the consistency between methods of determining α: on the left, the top line is the spike and the bottom the bubble, while it is opposite for the right panel. Also, a weighted running average of 20 % of the total number of points in the particular experiment is also performed (represented as solid and dashed lines on the plot) to smooth the data.

The time-dependent α value obtained using (5.4) is shown in figure 20, where, as was done for the immiscible experiments, $\dot{h}_{b/s}$ is determined using a central difference approximation. Also, as with the immiscible results, a weighted running average of 20 % of the total number of points in the particular experiment is also performed (represented as solid and dashed lines on the plot) to smooth the data and a dashed line is drawn representing the average α value obtained by the square-root method. As was similarly shown in the immiscible experiments, the square-root method agrees well with (5.4) at late time.

5.2.3. *Discussion and comparison of results*

A compilation of measured α values obtained from the experiments described here for both the immiscible and miscible experiments along with those obtained in prior studies is shown in table 1. As described above, good agreement is observed in the present study between the forced and unforced immiscible experiments, with differences less than the respective error estimates indicating that, even though there may be increased mode coupling in the unforced case, it does not appear to strongly alter the late-time self-similar behaviour. The values from the miscible experiments do not show the same level of agreement between the forced and unforced cases. Nevertheless, the forced and unforced measurements are within the range of their respective error estimates. This discrepancy may be expected, owing to difficulties when imaging the miscible experiments. It should be noted that, because of their much slower growth, the miscible experiments are much more strongly affected by edge effects, resulting in vortical structures at the front and back walls of the tank

https://doi.org/10.1017/jfm.2015.599 Published online by Cambridge University Press

Miscible experiments

Forced experiments			Unforced experiments		
This study				This study	
α_{spk}	α_{bub}	α_{ratio}	α_{spk}	α_{bub}	α_{ratio}
0.017 ± 0.008	0.023 ± 0.007	0.74 ± 0.41	0.047 ± 0.023	0.030 ± 0.008	1.57 ± 0.87

Immiscible experiments

This study					
α_{spk}	α_{bub}	α_{ratio}		α_{spk}	α_{bub}	α_{ratio}
0.057 ± 0.014	0.044 ± 0.009	1.30 ± 0.41	This study – unmatched nD	0.059 ± 0.002	0.047 ± 0.007	1.26 ± 0.19
			This study – matched nD	0.046 ± 0.011	0.039 ± 0.015	1.18 ± 0.53
			Youngs	0.086	0.066	1.3
			Kucherenko	0.070	0.055	1.27
			Dimonte	0.063	0.050	1.26

TABLE 1. Comparison of α values for experiments with Atwood number approximately 0.5. Here nD represents the refractive index at 589 nm. The refractive indices in this table are unmatched unless otherwise stated. The growth parameter α was extracted from mixing-layer width measurements using both the method of Dimonte & Schneider (1996) and that of Cabot & Cook (2006), where it was found that both methods yielded consistent results. Imaging for this study is performed by imaging refractive-index mismatch. Data from previous research are also compiled in the table (Youngs & Read 1983; Kucherenko *et al.* 1991; Youngs 1991; Dimonte & Schneider 2000).

caused by slight tank misalignments. These artifacts along with their associated effects on visualization are discussed in detail in Roberts (2012, 3.1.3) and are indicated by the larger uncertainty estimates for this set of experiments.

When comparing miscible and immiscible forced experiments, it is observed that the α values associated with the miscible ones are significantly smaller than those found in the immiscible experiments. Furthermore, the differences between the miscible and immiscible values are significantly larger than their associated error estimates, indicating that miscibility does play a statistically significant role in the growth parameter. This effect can be explained by the fact that molecular mixing will result in a lowering of the local effective Atwood number, as discussed by Cook *et al.* (2004). Cook *et al.* define the effective Atwood number as

$$A_e \equiv \frac{\rho_{rms}}{\langle\rho\rangle|_0}, \tag{5.5}$$

which they found to approach $A_e = 0.48A$ at late time in their miscible simulations. On the other hand, $A_e = A$ for immiscible fluids. Here $\langle\rho\rangle|_0$ represents the average density at the centre-plane ($z = 0$) and ρ_{rms} is the centre-plane root mean square density deviation. Cook *et al.* argue that molecular mixing results in a decrease in the local buoyancy force experienced by regions of lighter and heavier fluids near the zero plane in the mixing layer and thus should result in a lowering of the RTI turbulent growth rate. Cook *et al.* also hypothesize that this mechanism is the reason why their miscible simulations yield lower α values than all previous simulations that modelled the fluids as immiscible. The results presented here thus support Cook *et al.*'s hypothesis that miscibility results in a significant lowering of the RTI growth constant α. Furthermore, the factor of two difference between our miscible and immiscible α measurements agrees well with the difference between Cook *et al.*'s result and those of previous immiscible simulations.

6. Summary and conclusions

In this study, a system of two stratified liquids that is accelerated downwards at a rate greater than gravity is used to study the Rayleigh–Taylor instability. Experiments were performed using a weight-and-pulley apparatus, which produces a net acceleration of approximately $1g$, with fluid combinations having an Atwood number of 0.48. Owing to the large refractive index of the denser liquid for these large-Atwood-number experiments, the refractive index could not be matched. Thus, during an experiment the refractive-index mismatch is imaged. After the instability has progressed late enough in time, a mixing region develops. This mixing layer is assumed to be self-similar and turbulent. In this study, the effect of forcing and miscibility on the turbulent RTI was investigated. The initial conditions of these experiments were either forced to produce small-wavelength perturbations or left unforced (allowing small wavelengths, close in size to the fastest-growing wavelength, to grow). In addition, experiments were performed using miscible and immiscible liquid combinations. In all cases, we obtain a small-wavelength, finite-bandwidth initial perturbation consistent with the bubble-merger, mode-coupling case presented by Ramaprabhu *et al.* (2005).

The fact that the dominant scales appear to evolve in time proportionally with the mixing-layer width supports the assumption that the experiments are in the self-similar regime. Also, the Reynolds number was measured and compared to those obtained in earlier experimental studies, where it was verified that self-similarity was reached (from quantitative internal mixing region measurements). The Reynolds

numbers achieved in the present experiments were found to be similar to those found in earlier studies, implying that the flow in our experiments is sufficiently turbulent to be self-similar. Using the assumption of self-similarity, α values were obtained in a consistent manner for all the experiments presented here. The growth parameter α was extracted from mixing-layer width measurements using both the method of Dimonte & Schneider (1996) and that of Ristorcelli & Clark (2004) and Cabot & Cook (2006), where it was found that both methods yielded consistent results. For the immiscible forced experiments, it was found that $\alpha_s = 0.057 \pm 0.014$ and $\alpha_b = 0.044 \pm 0.009$, while for the immiscible unforced experiments $\alpha_s = 0.059 \pm 0.002$ and $\alpha_b = 0.047 \pm 0.007$. The α value differences between the forced and unforced experiments are within their respective error estimates, thus indicating that the differences in forcing the initial perturbations had no measurable effect in the resulting α values. For the miscible forced experiments, it was found that $\alpha_s = 0.017 \pm 0.008$ and $\alpha_b = 0.023 \pm 0.007$, while for the miscible unforced experiments, $\alpha_s = 0.047 \pm 0.023$ and $\alpha_b = 0.030 \pm 0.008$. It is particularly notable that the α values measured for the miscible experiments are significantly smaller than those of the immiscible experiments and that, for three of the four comparisons made, this difference is statistically significant based on the calculated confidence intervals, thus indicating that miscibility plays a role in the late-time turbulent instability growth. It is important to note that the effect of miscibility to reduce the value of α has never been observed experimentally. However, it supports the hypothesis of Cook *et al.* (2004) that molecular mixing results in the lowering of the buoyancy force experienced by light and heavy fluid regions near the centreline of the RTI mixing region. It is also significant that α values measured in the immiscible experiments of the present study are smaller than those measured in previous studies. This difference is most likely the result of the increased temporal resolution and the increased ensemble sizes used in the present study resulting in more accurate measurements of α at later times.

In this study we experimentally showed that imposing a small-wavelength initial perturbation on the interface does not significantly alter the value of α when compared to the case where a small-wavelength spectrum (from background noise perturbations) was allowed to develop due to viscous effects in the linear regime. This indicates that the form of a perturbation having a short enough wavelength and finite bandwidth does not affect the growth rate of the turbulent self-similar RTI and supports the conclusions put forward by Ramaprabhu *et al.* (2005). It was also found that miscibility does play a role in the turbulent RTI where the miscible experiments have a smaller growth rate than the immiscible ones.

Acknowledgements

This research was supported by Lawrence Livermore National Laboratory and by the National Nuclear Security Administration under the Stewardship Science Academic Alliances Program through DOE research grant no. DE-FG52-04NA00142.

REFERENCES

ANUCHINA, N. N., KUCHERENKO, YU. A., NEUVAZHAEV, V. E., OGIBINA, V. N., SHIBARSHOV, L. I. & YAKOVLEV, V. G. 1978 Turbulent mixing at an accelerating interface between liquids of different density. *Fluid Dyn.* **13** (6), 916–920.

BELLMAN, R. & PENNINGTON, R. H. 1954 Effects of surface tension and viscosity on Taylor instability. *Q. Appl. Maths* **12** (2), 151–162.

BETTI, R., GONCHAROV, V. N., MCCRORY, R. L. & VERDON, C. P. 1998 Growth rates of the ablative Rayleigh–Taylor instability in inertial confinement fusion. *Phys. Plasmas* **5** (5), 1446–1454.

CABOT, W. H. & COOK, A. W. 2006 Reynolds number effects on Rayleigh–Taylor instability with possible implications for type-Ia supernovae. *Nat. Phys.* **2** (8), 562–568.

CHANDRASEKHAR, S. 1961 *Hydrodynamic and Hydromagnetic Stability*. Dover.

CLARK, D. S., HAAN, S. W., COOK, A. W., EDWARDS, M. J., HAMMEL, B. A., KONING, J. M. & MARINAK, M. M. 2011 Short-wavelength and three-dimensional instability evolution in National Ignition Facility ignition capsule designs. *Phys. Plasmas* **18** (8), 082701.

COHEN, I. M. & KUNDU, P. K. 2004 *Fluid Mechanics*, 3rd edn. Elsevier.

COLE, R. L. & TANKIN, R. S. 1973 Experimental study of Taylor instability. *Phys. Fluids* **16** (11), 1810–1815.

COOK, A. W., CABOT, W. & MILLER, P. L. 2004 The mixing transition in Rayleigh–Taylor instability. *J. Fluid Mech.* **511**, 333–362.

DALZIEL, S. B. 1993 Rayleigh–Taylor instability – experiments with image-analysis. *Dyn. Atmos. Oceans* **20** (1–2), 127–153.

DALZIEL, S. B., LINDEN, P. F. & YOUNGS, D. L. 1999 Self-similarity and internal structure of turbulence induced by Rayleigh–Taylor instability. *J. Fluid Mech.* **399**, 1–48.

DIMONTE, G. 2004 Dependence of turbulent Rayleigh–Taylor instability on initial perturbations. *Phys. Rev.* E **69** (5, Part 2), 056305.

DIMONTE, G., MORRISON, J. J., HULSEY, S. D., NELSON, D., WEAVER, S., SUSOEFF, A. R., HAWKE, R. S., SCHNEIDER, M. B., BATTEAUX, J., LEE, D. & TICEHURST, J. 1996 A linear electric motor to study turbulent hydrodynamics. *Rev. Sci. Instrum.* **67** (1), 302–306.

DIMONTE, G., RAMAPRABHU, P. & ANDREWS, M. J. 2007 Rayleigh–Taylor instability with complex acceleration history. *Phys. Rev.* E **76** (4, Part 2), 046313.

DIMONTE, G. & SCHNEIDER, M. 1996 Turbulent Rayleigh–Taylor instability experiments with variable acceleration. *Phys. Rev.* E **54** (4), 3740–3743.

DIMONTE, G. & SCHNEIDER, M. 2000 Density ratio dependence of Rayleigh–Taylor mixing for sustained and impulsive acceleration histories. *Phys. Fluids* **12** (2), 304–321.

DIMONTE, G., YOUNGS, D. L., DIMITS, A., WEBER, S., MARINAK, M., WUNSCH, S., GARASI, C., ROBINSON, A., ANDREWS, M. J., RAMAPRABHU, P. *et al.* 2004 A comparative study of the turbulent Rayleigh–Taylor instability using high-resolution three-dimensional numerical simulations: the Alpha-Group collaboration. *Phys. Fluids* **16** (5), 1668–1693.

DUFF, R., HARLOW, F. & HIRT, C. 1962 Effects of diffusion on interface instability between gases. *Phys. Fluids* **5** (4), 417–425.

EMMONS, H. W., CHANG, C. T. & WATSON, B. C. 1960 Taylor instability of finite surface waves. *J. Fluid Mech.* **7** (2), 177–193.

FERMI, E. & NEUMANN, J. V. 1955 Taylor instability of incompressible liquids. United States Atomic Energy Commission: Unclassified, AECU-2979.

GHASEMIZAD, A., ZARRINGHALAM, H. & GHOLAMZADEH, L. 2009 The investigation of Rayleigh–Taylor instability growth rate in inertial confinement fusion. *J. Plasma Fusion Res.* **8**, 1234–1238.

GONCHAROV, V. N. 2002 Analytical model of nonlinear, single-mode, classical Rayleigh–Taylor instability at arbitrary Atwood numbers. *Phys. Rev. Lett.* **88** (13), 134502.

HERRMANN, M. C., TABAK, M. & LINDL, J. D. 2001 Ignition scaling laws and their application to capsule design. *Phys. Plasmas* **8** (5), 2296–2304.

JACOBS, J. W. & CATTON, I. 1988*a* Three-dimensional Rayleigh–Taylor instability. Part 1. Weakly nonlinear theory. *J. Fluid Mech.* **187**, 329–352.

JACOBS, J. W. & CATTON, I. 1988*b* Three-dimensional Rayleigh–Taylor instability. Part 2. Experiment. *J. Fluid Mech.* **187**, 353–371.

JACOBS, J. W. & DALZIEL, S. B. 2005 Rayleigh–Taylor instability in complex stratifications. *J. Fluid Mech.* **542**, 251–279.

KUCHERENKO, Y. A., PYLAEV, A. P., BALABIN, S. I., MURZAKOV, V. D., ARDASHOVA, R. I., POPOV, V. N., SAVEL'EV, V. E., KOMAROV, O. R., KOZELKOV, O. E., TYAKTEV, A. A. *et al.* 1997*a* Experimental investigation into the behavior of inertial motion for different Atwood numbers. In *Proceedings of the Sixth International Workshop on The Physics of Compressible Turbulent Mixing*, pp. 282–288.

KUCHERENKO, Y. A., PYLAEV, A. P., MURZAKOV, V. D., BELOMESTNIH, A. V., POPOV, V. N. & TYAKTEV, A. A. 2001 Experimental study into Rayleigh–Taylor turbulent mixing zone heterogenous structure. In *Proceedings of the Eighth International Workshop on The Physics of Compressible Turbulent Mixing*, RFNC-VNIITF.

KUCHERENKO, Y. A., PYLAEV, A. P., MURZAKOV, V. D., POPOV, V. N., KOMAROV, O. R., SAVELEV, V. E., CHERRET, R. & HAAS, J. F. 1997*b* Experimental study into the asymptotic stage of the separation of the turbulized mixtures in gravitationally stable mode. *Laser Part. Beams* **15** (1), 17–23; Zababakhin's Scientific Talks, Snezhinsk, Russia, 16–20 September 1995.

KUCHERENKO, Y. A., SHIBARSHOV, L. I., CHITAIKIN, V. I., BALABIN, S. I. & PYLAEV, A. P. 1991 Experimental study of the gravitational turbulent mixing self-similar mode. In *Proceedings of the 3rd International Workshop on the Physics of Compressible Turbulent Mixing*, pp. 427–454.

LAWRIE, A. G. W. & DALZIEL, S. B. 2011 Turbulent diffusion in tall tubes. I. Models for Rayleigh–Taylor instability. *Phys. Fluids* **23** (8), 085109.

LAYZER, D. 1955 On the instability of superposed fluids in a gravitational field. *Astrophys. J.* **122** (1), 1–12.

LEWIS, D. J. 1950 The instability of liquid surfaces when accelerated in a direction perpendicular to their planes. 2. *Proc. R. Soc. Lond.* A **202** (1068), 81–96.

LINDEN, P. F. & REDONDO, J. M. 1991 Molecular mixing in the Rayleigh–Taylor instability. Part I: Global mixing. *Phys. Fluids* A **3** (5), 1269–1277.

MUESCHKE, N. J., SCHILLING, O., YOUNGS, D. L. & ANDREWS, M. J. 2009 Measurements of molecular mixing in a high-Schmidt-number Rayleigh–Taylor mixing layer. *J. Fluid Mech.* **632**, 17–48.

NEUVAZHAEV, V. E. & YAKOVLEV, V. G. 1976*a* Numerical gas-dynamical calculation of turbulent mixing of the interface. *J. Comput. Math. Phys. USSR* **16** (2), 154–165.

NEUVAZHAEV, V. E. & YAKOVLEV, V. G. 1976*b* Theory of turbulent mixing at the interface of fluids in a gravity field. *J. Appl. Mech. Tech. Phys.* **17** (4), 513–519.

OLSON, D. H. & JACOBS, J. W. 2009 Experimental study of Rayleigh–Taylor instability with a complex initial perturbation. *Phys. Fluids* **21** (3), 034103.

ORON, D., ARAZI, L., KARTOON, D., RIKANATI, A., ALON, U. & SHVARTS, D. 2001 Dimensionality dependence of the Rayleigh–Taylor and Richtmyer–Meshkov instability late-time scaling laws. *Phys. Plasmas* **8** (6), 2883–2889.

PARSONS, P. W. & ESTRADA, F. J. 1942 Changes in volume on mixing solutions. *Ind. Engng Chem.* **34**, 949–952.

POLING, B. 2001 *The Properties of Gases and Liquids*. McGraw-Hill.

RAMAPRABHU, P. & ANDREWS, M. J. 2003 Simultaneous measurements of velocity and density in buoyancy-driven mixing. *Exp. Fluids* **34** (1), 98–106.

RAMAPRABHU, P. & ANDREWS, M. J. 2004 Experimental investigation of Rayleigh–Taylor mixing at small Atwood numbers. *J. Fluid Mech.* **502**, 233–271.

RAMAPRABHU, P., DIMONTE, G. & ANDREWS, M. J. 2005 A numerical study of the influence of initial perturbations on the turbulent Rayleigh–Taylor instability. *J. Fluid Mech.* **536**, 285–319.

RATAFIA, M. 1973 Experimental investigation of Rayleigh–Taylor instability. *Phys. Fluids* **16** (8), 1207–1210.

RAYLEIGH, LORD 1883 Investigation of the character of the equilibrium of an incompressible heavy fluid of variable density. In *Scientific Papers*, vol. 2, pp. 200–207. Cambridge University Press.

READ, K. I. 1984 Experimental investigation of turbulent mixing by Rayleigh–Taylor instability. *Physica* D **12** (1–3), 45–58.

RISTORCELLI, J. R. & CLARK, T. T. 2004 Rayleigh–Taylor turbulence: self-similar analysis and direct numerical simulations. *J. Fluid Mech.* **507**, 213–253.

ROBERTS, M. S. 2012 Experiments and simulations on the incompressible, Rayleigh–Taylor instability with small wavelength initial perturbations. PhD thesis, The University of Arizona.

SCHNEIDER, M. B., DIMONTE, G. & REMINGTON, B. 1998 Large and small scale structure in Rayleigh–Taylor mixing. *Phys. Rev. Lett.* **80** (16), 3507–3510.

SETTLES, G. S. 1999 Schlieren and shadowgraph imaging in the great outdoors. In *Proceedings of PSFVIP-2*, PF302.

SHARP, D. H. 1984 An overview of Rayleigh–Taylor instability. *Physica* D **12** (1–3), 3–18.

SNIDER, D. M. & ANDREWS, M. J. 1994 Rayleigh–Taylor and shear-driven mixing with an unstable thermal stratification. *Phys. Fluids* **6** (10), 3324–3334.

TANAKA, Y., YAMAMOTO, T., SATOMI, Y., KUBOTA, H. & MAKITA, T. 1977 Specific volume and viscosity of ethanol–water mixtures under high pressure. *Rev. Phys. Chem. Japan* **47**, 12–24.

TAYLOR, G. I. 1950 The instability of liquid surfaces when accelerated in a direction perpendicular to their planes. I. *Proc. R. Soc. Lond.* A **201**, 192–196.

WADDELL, J. T. 1999 Experimental study of the Rayleigh–Taylor instability of miscible liquids. Master's thesis, University of Arizona.

WADDELL, J. T., NIEDERHAUS, C. E. & JACOBS, J. W. 2001 Experimental study of the Rayleigh–Taylor instability: low Atwood number liquid system with single-mode initial perturbations. *Phys. Fluids* **13** (5), 1263–1273.

WILKINSON, J. P. & JACOBS, J. W. 2007 Experimental study of the single-mode three-dimensional Rayleigh–Taylor instability. *Phys. Fluids* **19** (12), 124102.

YOUNGS, D. 1984 Numerical simulation of turbulent mixing by Rayleigh–Taylor instability. *Physica* D **12**, 32–44.

YOUNGS, D. L. 1989 Modeling turbulent mixing by Rayleigh–Taylor instability. *Physica* D **37** (1–3), 270–287.

YOUNGS, D. L. 1991 Three-dimensional numerical simulation of turbulent mixing by Rayleigh–Taylor instability. *Phys. Fluids* A **3** (5, Part 2), 1312–1320; International Symposium on Fluid Mechanics of Stirring and Mixing, University of California–San Diego, La Jolla, CA, 20–24 August 1990.

YOUNGS, D. L. 1994 Numerical-simulation of mixing by Rayleigh–Taylor and Richtmyer–Meshkov instabilities. *Laser Part. Beams* **12** (4), 725–750.

YOUNGS, D. L. & READ, K. I. 1983, Experimental investigation of turbulent mixing by Rayleigh–Taylor instability. Atomic Weapons Research Establishment Report (O11/83).